

Modeling the morphological diversity of impact craters on icy satellites

Laurel E. Senft and Sarah T. Stewart

Department of Earth and Planetary Sciences
Harvard University
20 Oxford Street
Cambridge, MA 02138

Senft: laurelsenft@gmail.com, 857-998-1685

Stewart: sstewart@eps.harvard.edu, 617-496-6462

Submitted to Icarus June, 2009

Revised March, 2011

Accepted April, 2011

13 Figures, and 1 Table

Online Supplemental Materials: 2 pages, 1 Table, 2 Figures, 13 Quicktime animations

Proposed running head: Cratering in ice

Direct editorial correspondence and proof to: Sarah Stewart

Keywords: cratering, ices, Ganymede, Callisto, interiors

Abstract

Impact craters on icy satellites display a wide range of morphologies, some of which have no counterpart on rocky bodies. Numerical simulation studies have struggled to reproduce the diversity of features, such as central pits and transitions in crater depth with increasing diameter, observed on the icy Galilean satellites. The transitions in crater depth (at diameters of about 26 and 150 km on Ganymede and Callisto) have been interpreted as reflecting subsurface structure. Using the CTH shock physics code, we model the formation of craters with diameters between 400 m and about 200 km on Ganymede using different subsurface temperature profiles. Our calculations include recent improvements in the model equation of state for H₂O and quasi-static strength parameters for ice. We find that the shock-induced formation of dense high-pressure polymorphs (ices VI and VII) creates a gap in the crater excavation flow, which we call discontinuous excavation. For craters larger than about 20 km, discontinuous excavation concentrates a hot plug of material (>270 K and mostly on the melting curve) in the center of the crater floor. The size and occurrence of the hot plug are in good agreement with the observed characteristics of central pit craters, and we propose that a genetic link exists between them. We also derive depth vs. diameter curves for different internal temperature profiles. In a 120 K isothermal crust, calculated craters larger than about 30 km diameter are deeper than observed and do not reproduce the transition at about 26 km diameter. Calculated crater depths are shallower and in good agreement with observations between about 30 and 150 km diameter using a warm thermal gradient representing a convective interior. Hence, the depth-to-diameter transition at about 26 km reflects thermal weakening of ice. Finally, simulation results generally support the hypothesis that the anomalous interior morphologies for craters larger than 100 km are related to the presence of a subsurface ocean.

1. Introduction

Impact craters are widespread throughout the solar system and are thus useful probes into planetary subsurfaces. The crater morphology resulting from the impact of an asteroid or comet onto a planetary body is primarily a function of the impactor kinetic energy (velocity and mass), the target composition, and the gravity of the target. Because the icy Galilean satellites (Europa, Ganymede, and Callisto) have a similar gravitational acceleration as Earth's moon, it could be expected that craters of the same size on these bodies would show similar morphologies. Yet craters larger than a few km on the icy satellites are generally shallower than their lunar counterparts, lack peak rings, and display unique morphologies (e.g., central pits, central domes, anomalous forms, and palimpsests) that have no lunar counterpart (Bray et al., 2008; Croft, 1981; Croft, 1983; Moore and Malin, 1988; Moore et al., 2001; Moore et al., 2004; Passey and Shoemaker, 1982; Schenk, 1991; Schenk, 1993; Schenk, 2002; Schenk et al., 2004; Schenk and Turtle, 2009; Smith et al., 1979).

The major differences between craters on icy satellites and the moon are illustrated by crater depth and diameter measurements and morphological classifications from Schenk (2002), shown in Figure 1. Simple craters on the icy satellites (black dots in Figure 1) show the traditional bowl shape with depth to diameter ratios similar to those for the moon (thick black line). However the transition from simple to complex craters occurs at smaller crater diameters on the icy satellites (2-3 km, Transition I) than for the moon (15 km, (Pike, 1976)). The simple to complex transition scales with gravity and the strength of the surface materials; hence, the difference in Transition I is attributed to the surface composition: rock for the moon and primarily H₂O ice for the icy Galilean satellites. For Ganymede and Callisto, after Transition I, the crater depths increase with diameter (open circles in Figure 1) until a second kink is reached at diameters of about 26 km (Transition II). At Transition II, crater depths become constant or slowly decrease with diameter and the dominant morphology transitions from central peaks to central pits and central domes (crosses in Figure 1). There is no corresponding transition in the lunar depth versus diameter data and no corresponding lunar crater

morphologies. For craters larger than about 150 km (Transition III) on Ganymede and Callisto (error bars in Figure 1), crater morphologies become anomalous and extremely shallow. On the Moon, the transition to basins begins around 100-200 km, where central peak morphologies transition to peak-ring morphologies (Williams and Zuber, 1998). However, note that the degree of structural equivalence between basins on the Moon and icy satellites is not well understood. The morphological characteristics for craters on Ganymede and Callisto are essentially the same. However, European craters differ from craters on Ganymede and Callisto, with Transitions II and III occurring at smaller crater diameters (about 8 and 30 km, respectively). Furthermore, there are no central pit craters on Europa as almost no craters are preserved in this size range (Schenk and Turtle, 2009).

Schenk (2002) proposed that Transition II is a result of a brittle to ductile transition within the solid ice shell and that Transition III is related to the depth to the ocean. He hypothesized that the differences between the crater morphologies on Europa and Ganymede/Callisto are due to a thinner and warmer ice shell and/or a shallower ocean on Europa. Based on preliminary simulations that indicated that a subsurface ocean is breached when its depth is comparable to the transient crater diameter (Turtle and Ivanov, 2002), Schenk estimated the minimum thickness of the solid ice shells to be 19-25 km for Europa and about 80 km for Ganymede and Callisto.

It is clear that understanding the cratering process on an icy surface will lead to a better interpretation of what causes the unique crater morphologies on the icy Galilean satellites, and better constraints on the internal structures of these bodies. The internal structures of the icy Galilean satellites are of interest because of the presence of subsurface oceans (Showman and Malhotra, 1999; Spohn and Schubert, 2003). In particular, the solid ice shell on Europa may be thin enough to support life in the ocean (Billings and Kattenhorn, 2005; Chyba, 2000). However, the thickness of Europa's ice shell remains the focus of much debate (Billings and Kattenhorn, 2005).

Numerical modeling of impact cratering on the icy satellites have been used to infer the minimum depth to Europa's ocean (Turtle and Pierazzo, 2001), to calculate melt production on Titan (Artemieva and Lunine, 2003; Artemieva and Lunine, 2005), and to investigate the crater collapse process in ice (Bray et al., 2008). Turtle and Pierazzo (2001) modeled the early stage of impact and calculated the depths of melting below craters of different sizes and in targets with varying depths to an ocean. Based on the assumption that central peaks cannot form in craters where the melt zones penetrate to the subsurface ocean, they constrained the crust to be at least 3 to 4 km thick. Bray et al. (2008) simulated the formation of approximately 20-km diameter craters on Ganymede to fit the parameters for different strength-weakening models that control the final stage of crater formation. They found that the strength-weakening parameters for Ganymede are similar to those fitted to the moon. Additionally, Artemieva and Lunine (2003; 2005) used 3D numerical simulations of the early stages of impacts onto ice to estimate the amount of liquid water that may have been generated on the Saturnian moon Titan. They found that very early on in Titan's history, a global liquid layer may have been present, but at later times, impact-generated liquid was local and transient.

Accurate modeling of crater formation in ice requires a robust equation of state and temperature-dependent strength model. The major limitation of previous studies of cratering in ice has been the equation of state (EOS) model. In general, EOS models for H₂O (such as ANEOS (Thompson and Lauson, 1972; Turtle and Pierazzo, 2001), Mie-Grüneisen, and Tillotson (Appendix II in Melosh, 1989)) have been highly simplified, neglecting the high-pressure solid phases and inaccurately representing phase boundaries.

In this work, we model the formation of impact craters with diameters between 400 m and about 200 km on Ganymede using different subsurface temperature profiles. The simulations utilize a new EOS model for H₂O, the 5-Phase EOS, which includes high-pressure solid phases and accurate melting and vaporization curves. We model the entire cratering process, from impact to final morphology, using an updated rheological model for ice. The goals of this study are to (1) improve our

understanding of the mechanics of crater formation in ice (including the sensitivity to the EOS and strength model) and (2) to identify the process(es) that lead to the diversity of crater morphologies on icy satellites.

2. Method

We conducted two-dimensional, axisymmetric simulations of crater formation on Ganymede. The projectile and targets were composed of pure H₂O. While Ganymede (surface gravity of 1.43 m/s²) is believed to be differentiated (with a nearly pure H₂O surface), Callisto's (1.32 m/s²) internal structure is more ambiguous (e.g., Schubert et al., 2004). The results of this work also apply to Callisto if its crust is predominantly composed of H₂O ice. Projectile diameters ranged from 10 m to 20 km. The nominal impact velocity was 15 km/s, similar to estimates of the mean impact velocities on the icy Galilean satellites (21 km/s on Ganymede and 16 km/s on Callisto for the impact of Jupiter family comets, which comprise >90% of impactors on these satellites (Zahnle et al., 1998)). Final crater (rim-to-rim) diameters ranged from 400 m to about 200 km.

We varied the internal temperature profile of Ganymede. The surface temperature was assumed to be 120 K (approximately the equilibrium mid-latitude surface temperature). Two thermal profiles were considered: an end-member "cold" isothermal crust and a "warm" thermal gradient to represent a convective interior. The warm case is assumed to have a gradient of 20 K/km through the lithosphere (6.5 km thick) and a convecting ice interior at 250 K. These temperature profiles are consistent with estimates of the early thermal gradient and lithospheric thickness on Ganymede (Golombek and Banerdt, 1986; Luttrell and Sandwell, 2006). Two sets of simulations were also conducted with the added complexity of a 275 K ocean at depths of 25 and 50 km, below the convective lid (at 250 K). The ocean extends to the bottom of the computational mesh. We model the boundary between the convective ice and the ocean as an abrupt transition; in actuality, the boundary layer should have a small width (Schubert et al., 2004). The projectile temperature was 120 K in all cases.

Cratering simulations were conducted using the widely-used CTH shock physics code (version 8) (McGlaun et al., 1990), which we have extended to include strength models appropriate for planetary impact problems (Senft and Stewart, 2007). The resolution of the computational mesh is fixed in the region of crater formation, and the resolution is allowed to increase in the margins of the calculation domain using the adaptive mesh refinement feature (Crawford, 1999). The maximum resolution of each simulation was at least 40 cells across the diameter of the projectile. Massless, Lagrangian tracer particles are embedded in horizontal rows to track the stratigraphic deformation and thermodynamic histories of the target material.

We utilize the quasi-static strength model of Collins et al. (2004) (Senft and Stewart, 2007; Senft and Stewart, 2008). In this model, a pressure-dependent shear strength is degraded from an intact curve to a damaged (fractured curve) with the accumulation of damage (which is a function of integrated plastic shear strain). The shear strength is thermally degraded with a pressure-dependent melting curve that matches the melting curve for H₂O ice. Tensile strength is also degraded with damage, and void is added under tensile failure to simulate fracturing. The strength parameters for ice are derived in Senft and Stewart (2008) by fitting to experimental data on the quasi-static shear strength, friction, and dynamic tensile strength. The parameters are slightly modified from Senft and Stewart (2008) to better match the colder temperatures on Ganymede compared to Mars (see Table 1).

To achieve the appropriate amount of collapse, a transient weakening mechanism is needed for complex craters. The weakening process is still debated (Senft and Stewart, 2009); however, the specific model should not affect the general results presented in this paper (see Section 4.4). We use the block model approximation (Melosh and Ivanov, 1999) of acoustic fluidization (Melosh, 1979), whereby acoustic waves generated by the impact periodically increase and decrease the overburden pressure (temporarily allowing the material to fail). Averaged over time, the bulk rheology of the weakened

material is approximated by a Bingham plastic (a material that behaves as a rigid solid below the yield stress, but as a viscous fluid above the yield stress). The effective viscosity and a decay time (representing the characteristic decay time of the acoustic waves) are the two main parameters of the model. Because the acoustic fluidization parameters are unconstrained by laboratory experiments, they are generally chosen by fitting to observed crater depth versus diameter curves (e.g., Collins, 2002; Wünnemann and Ivanov, 2003). However, using this method to choose parameters for Ganymede (tweaking the parameters until a perfect match is reached) would obscure the effect of other variables, such as the thermal profile and equation of state. There is no physical reason for greatly different acoustic fluidization parameters in ice and rock, and a recent study (Bray et al., 2008) argues that the crater collapse process is similar on Ganymede and the moon based on the gross similarity in complex crater morphologies for diameters less than 12 km. The same study successfully reproduced the observed morphology of approximately 20-km diameter Ganymedean craters using acoustic fluidization parameters similar to the moon (no other sizes were modeled). Thus, in this work, we used acoustic fluidization parameters as determined for the moon (Wünnemann and Ivanov, 2003).

The projectile and target were modeled using the tabular 5-Phase equation of state (EOS) for H₂O (Senft and Stewart, 2008). This EOS has been validated with experimental data (Senft and Stewart, 2008; Stewart et al., 2008). The 5-Phase EOS includes three solid phases (ices Ih, VI, and VII), liquid, and vapor. In reality, H₂O forms at least 11 stable phases (Petrenko and Whitworth, 1999); however, some phases are not created during shock compression (Stewart and Ahrens, 2005). Hence, the model EOS artificially extends the ice VI region to include the ice II, V, and III regions and the ice VII region to include the ice VIII region. The EOS of the phases and unmodified phase boundaries are experimentally determined; for more details see the Appendix and Senft and Stewart (2008). Note that the EOS as presented in Senft and Stewart (2008) contains liquid and solid (ice Ih) tension regions which overlap in temperature versus density space with regions of liquid-vapor and ice Ih-vapor equilibrium, respectively. Since we are interested in the late stage evolution of material on the phase boundaries, we have removed the tension regions from the table (the boundaries are now pure equilibrium). At present, we are unable to model in a single simulation both the release into tension behind the shock wave at early times and the (quasi-)equilibrium compression/decompression of material during crater collapse. We conducted tests to compare cratering simulations with and without tension. The crater formation process and resulting crater sizes were indistinguishable, although the thermodynamic paths of the material are different at early times. The equilibrium table (no tension) is more appropriate for the processes discussed in this work. The EOS does not include phase change kinetics (see discussion in section 4.4).

For comparison, we present a simulation using a Mie-Grüneisen equation of state for ice Ih. This EOS does not include any phase changes and utilizes a constant specific heat capacity to calculate temperature. Hence, the temperatures are unreliable. The Mie-Grüneisen EOS (appendix in Melosh, 1989) parameters are: 930 kg/m³ for the initial density, 3 km/s for the bulk sound speed, 1 for the linear slope between shock velocity and shock particle velocity, 1 for the Grüneisen parameter, and 1.98e17 J/kg/K for the specific heat capacity. This EOS allows material to go into tension and the same strength model is used as in the 5-Phase EOS simulations.

In all simulations, very low density material (<0.0001 g/cm³) is discarded to allow for reasonable time steps during the calculation.

3. Results

3.1 Discontinuous Excavation: Phase Changes and Hot Plug Formation

This work is the first to use a H₂O equation of state with high-pressure solid phases in simulations of crater formation on icy satellites. We find that the shock-induced formation of dense high-pressure polymorphs creates a discontinuity in the excavation flow. Over a certain size range, the

highly-shocked material that is interior to the discontinuity is concentrated in a hot, partially liquid plug in the crater floor during crater collapse. This previously unrecognized phenomenon, which we call *discontinuous excavation*, arises from the exceptional polymorphism of H₂O.

The differences between discontinuous excavation and classical crater excavation are illustrated in the simulations shown in Figure 2 and the schematic in Figure 3. Figure 2 presents a time series from a simulation of a 2-km diameter projectile impacting at 15 km/s onto a 120 K isothermal Ganymedeian crust. The final crater is about 39 km in diameter. The left column presents the results using the 5-Phase EOS; the right column presents the results using a Mie-Grüneisen EOS. Initially horizontal rows of tracer particles (black dots and lines in 2A-D and 2F-I) display the stratigraphic deformation. Animations are available in the online supplemental material.

The simulation using the Mie-Grüneisen EOS illustrates classical crater excavation (Figure 2F-J) (c.f. Melosh, 1989). After the initial contact and compression stage, the shock wave travels through the target as a hemispherical shell of high pressure and density (called the detached shock, Figure 2F). The material behind the shock wave is released to ambient pressure, setting up the classical excavation flow field that generates a hemispherical transient crater and inverted cone ejecta curtain (Figure 2G and 2H). The transient crater collapses under the force of gravity, and the transiently weakened material (from acoustic fluidization) flows inward and upwards, producing a shallow final crater with uplifted stratigraphy beneath the crater floor (Figure 2I). The deep narrow line of hot temperature material presented in Figure 2J represents the characteristic width of artifacts that arise along the center line in a two-dimensional axisymmetric calculation. Recall that the temperatures calculated with the Mie-Grüneisen EOS are unrealistic.

In contrast, the time series for the simulation using the 5-Phase EOS displays a gap, or discontinuity, in the excavation flow field. The amplitude of the shock wave decays during propagation into the target. As a result, ice Ih is shocked to progressively lower pressure (and temperature) phases with increasing distance from the impact point. The phase in the shocked state is a supercritical fluid at the impact site, followed by liquid, then high-pressure ice phases (ices VII and VI), and finally simply shock-compressed ice Ih with increasing distance (Figures 2A and 3A).

Rarefaction waves from the free surfaces decompress the shocked material. During impact cratering in ice, the release wave travels through layers of different phases, with a strong impedance contrast (density times sound speed) at the liquid-ice VII and ice VI-ice Ih boundaries. The impedance mismatch leads to wave reflections that generate the discontinuity in the excavation flow at the ice VI-ice Ih boundary. In addition, because transformation from the high-pressure solid phases back to ice Ih requires a large volume increase (e.g., about 30% from ice VI to ice Ih), full release of the high-pressure polymorphs is delayed until the volume change can be accommodated in the excavation flow. Thus in Figure 2A, the shock front has proceeded to about 12 km away from the surface, but material far behind the shock wave remains at high density and pressure (red shell). As the excavation flow relieves the overburden pressure, the transformation back to ice Ih occurs progressively from the free surface to greater depths. The time history of an example parcel of material compressed to ice VI is shown on a pressure-temperature phase diagram in Figure 4A (corresponding to the triangle symbol in Figure 2A-D). This parcel was shocked to ice VI and then released to the (artificial) ice Ih-VI phase boundary where it remained for several seconds; the material eventually transformed into ice Ih and decompressed to the sublimation curve before being re-compressed during crater collapse.

The large differences in the shock loading and unloading paths between adjacent material shocked to different phases disrupts the excavation flow (see Appendix). In addition, the impedance mismatch between the high pressure ice phases and lower-density phases (supercritical fluid and ice Ih) produce wave reflections that aid in the deceleration of the most highly shocked material. The net effect of these processes is that the fully released particle velocities of the material shocked to high pressure phases are slower than the material shocked within the ice Ih field (exterior to the

discontinuity). As a result, the most highly shocked material does not follow the main excavation flow, but lags behind, leading to the formation of a gap in the flow field (see Figures 2B and 2C). The material adjacent to the gap intersects the sublimation curve while decompressing to the low ambient pressure, producing the vapor in the gap (gray material in Figure 2B).

Rather than lining the transient crater cavity (as in Figure 2H), the highly shocked material is decelerated and remains temporarily suspended within the transient crater (Figure 2C). This material slowly falls to the crater floor and is compressed by the collapsing crater walls, forming a central plug in the crater floor (Figure 2D and 3C). This central plug is composed of material that was shocked to ice VI, ice VII, and supercritical fluid. Note that, in this example, the material within the central plug is near its original depth rather than forming a broad centrally uplifted zone (as in Figure 2I). We refer to the stratigraphic discontinuity as the central plug. Within the central plug is a smaller plug of hot material that lies on the melt curve (Figures 2E and 3C). We define the hot plug of material by the 270 K temperature contour. Because of the varying pressure field during crater collapse, material near the liquid phase boundary tends to fluctuate above and below the boundary. The fluctuations are probably accentuated by the use of a tabular equation of state. Hence, it is difficult to reliably calculate the exact amount of material that reaches the melting point. In the simulations, the volume of material with temperatures above 270 K remained fairly constant and at times nearly identical to the volume of material above 273 K. An example time history for a parcel of hot plug material is presented in Figure 4B (corresponding to the square symbol in Figure 2A-D). In this case, the parcel initially releases to the saturation vapor curve and continues to cool and decompress by creating vapor (as observed experimentally in Stewart et al. (2008)). In this case, the material is recompressed by collapsing to the ground after passing through the triple point.

Note that the width of the hot plug (~16 km) is much larger than the center line artifact (~2 km) observed in Figure 2J. Thus, while some of the material in the hot plug in the 5-Phase EOS calculation may be produced because of a centerline artifact, the majority is not. The mass of the hot plug depends on the impact energy and the impact velocity (see section 4.2). If the velocity is too low, then the peak pressures generated by the impact will not be high enough to induce (incipient) melting. However, as the impact velocity increases, the pressure decay profile becomes steeper (Pierazzo et al., 1997) (because more energy is portioned into vaporization), leading to smaller hot plugs. Because crater size is related to impact energy, the mass of the hot plug also scales with the crater diameter (Figure 5). The hot plug volume is only slightly sensitive to initially cold and warm thermal profiles.

These simulations utilize a simplified phase diagram for H₂O and assume equilibrium behavior upon release of the high-pressure phases. These limitations will be discussed in section 4.4.

The general phenomenon of discontinuous excavation has been observed in previous simulations of impact cratering in layered targets (Ormo et al., 2002; Senft and Stewart, 2007; Senft and Stewart, 2008). For example, impacts through an ocean or ice layer generated nested craters and ejecta curtains. In these previous studies, the discontinuous excavation arose from pre-existing impedance contrasts in the target. In this study, the discontinuous excavation flow occurs in an initially homogenous target and arises from shock-induced phase changes during the impact event.

3.2 Depth vs. Diameter

Our simulations of crater formation utilize independently derived input parameters: quasi-static strength parameters determined by laboratory experiments, acoustic fluidization parameters fitted to lunar data, and an equation of state based on laboratory data. Thus, these simulations of impact cratering in ice are predictive rather than fitted to observations. We find that the final geometries of the simulated craters are in good agreement with observations. In Figure 6, we compare the depth of the simulated craters to measurements of craters on Ganymede and the moon. The shaded area represents the scatter in the measurements from Schenk (2002) (Figure 1B; shaded area does not include error bars on the data points). Our simulated crater geometries lie within or adjacent (within

the error bars) to the observed scatter in the observations (with differences in thermal profiles discussed below).

To calculate the depths and diameters for the simulated craters, we define the topographic profile by identifying cells with 50% of full density. The rim-to-rim diameter is determined by finding the highest rim point, and the rim-to-floor depth is determined by subtracting the deepest floor point from the highest rim point (ignoring obvious small-scale blips in the topography). Because we use the deepest floor point and not an average over some area of the crater floor, our measurements should be slightly biased toward deeper depths compared to values derived from lower spatial resolution observations (and ignoring post-formation modification). The slightly shallower simulated simple craters may be the result of a quasi-static shear strength that is larger than reality (which limits penetration of the projectile) or too much slumping of the crater walls (e.g., quasi-static shear strength that is weaker than reality). The depths of large craters are sensitive to the initial thermal gradient because of the temperature-dependent shear strength.

3.3 Cold vs. Warm Thermal Profiles

The geometry of craters smaller than about 30 km is not sensitive to the cold vs. warm thermal profile (Figure 6). We do not consider the 0.1 km difference significant for the 3-km diameter cases. For larger craters, there are significant differences between craters formed in the cold versus the warm thermal profiles. Examples of crater formation by a 5-km diameter projectile impacting at 15 km/s are shown in Figure 7; the final crater diameters are about 105 and 145 km for the cold and warm thermal gradient cases, respectively. The phenomenon of discontinuous excavation is also clearly seen in these larger impact craters (note that the first time step at 45 seconds is after full release of the high pressure phases). For the crater formed in the cold case, the central plug falls to the crater floor and is not uplifted much during crater collapse. Uplift occurs around the plug, and part of the plug is squeezed upwards as the walls collapse (Figure 7; 200 and 400s).

In contrast, the central plug falls more quickly to the crater floor in the warm thermal gradient simulation. A smaller volume of high pressure phases forms during shock compression at higher initial temperatures. The slightly different loading and release paths lead to a smaller velocity difference at the discontinuity in the warm case. The most highly shocked material then partially lines the transient crater cavity. A very large central peak is created that overshoots the original surface level and then collapses, going through a few oscillations before crater formation is complete. Note that the oscillations in the large central peak effectively mix the original stratigraphy over a wide and deep region in the crater floor. In addition, the most highly shocked material is not resting at the surface.

The enhanced collapse in the warm thermal gradient, ultimately forming a larger shallower crater compared to the cold case, is a result of the strong temperature dependence on the strength of ice at relatively low confining pressures. We use a hyperbolic tangent form for the strength reduction; as a result of this dependence, the strength at 210 K is about half the strength at 120 K, and the strength at 250 K is about 17% the strength at 120 K.

3.3 Subsurface Oceans

Adding a subsurface ocean greatly increases the complexity of the cratering process. Example simulations with a subsurface ocean at 25 and 50 km depth are shown in Figure 8 (note that the ice lid overlying the ocean has a warm thermal gradient). In these cases, a 10-km diameter projectile impacting at 15 km/s produces very large final craters, but the rim is difficult to define. Note that discontinuous excavation is evident and affects the flow field in the solid portion of the satellite, although this phenomenon is secondary to the crater collapse process in controlling the final crater morphology. Discontinuous excavation is not observed in the ocean portion of the impacted material because liquid H₂O does not shock to solid phases in a single shock event (Stewart and Ahrens, 2005).

When the boundary between the icy crust and the ocean is breached (Figure 8A), or when excavation reaches the ice/water boundary (Figure 8F), the floor rebounds upwards dramatically (Figure

8B and 8G). The overshooting central peak then collapses with enough energy to form a second cavity (Figure 8C and 8H). Next, solid ice collapses in from the sides to fill this second cavity (Figure 8C and 8H). In contrast to terrestrial cratering, the melt produced in icy impacts is negatively buoyant; hence, the most highly shocked material sinks below the solid layer during collapse of the walls of the second cavity. Note that the exact morphology of the sinking material is probably affected by center line artifacts.

The center of the crater continues to oscillate long after the time of impact. As a result, the calculation is more susceptible to errors introduced by the boundaries in the simulation. Furthermore, the observed topography of anomalous basins on icy satellites is also affected by the long term cooling and freezing of the disrupted near-surface layers and viscous relaxation (although the latter probably only applies to the oldest craters (Dombard and McKinnon, 2000; Schenk et al., 2004)). For these reasons, it is difficult to derive a robust depth for comparison to observations, and the ocean simulations are not plotted on Figure 6. It is possible that anomalous craters may also be produced before the ocean is penetrated. Further investigation of the effect of oceans on crater morphology is left for future work.

In general, the subsurface ocean simulations support the hypothesis that final crater depths should be shallower due to the accentuated crater collapse when the ocean is breached compared to crater formation completely within the solid surface layer.

4. Discussion

4.1 Transitions in Crater Depth vs. Diameter

Schenk (2002) observed three transitions in the depth versus diameter curves for craters on the icy satellites. The first transition (Transition I) is the simple to complex crater transition, when gravity starts to dominate the crater collapse process (as opposed to material strength). The second transition (Transition II) marks a change in the depth versus diameter curves from increasing depth with diameter to constant or slightly decreasing depth with diameter. Our simulations show that depths continue to increase with diameter in a cold isothermal crust; however, for a warm thermal gradient, there is a rollover in the depth versus diameter curve, and depths began to decrease with diameter (Figure 6). This rollover is caused by the strong dependence of ice strength on temperature. Schenk interpreted Transition II to result from a ductile layer at depth. Note that because of the differences between strength models used in cratering studies versus planetary interior models, it is difficult to relate our results to an abrupt transition to a ductile layer at depth. On Europa, Transition II occurs at smaller crater diameters than it does on Ganymede and Callisto, and the decrease in crater depth with increasing diameter following the transition is steeper. These differences are probably a result of a steeper thermal gradient on Europa.

Transition III is thought to result from the influence of an ocean at depth (Schenk, 2002). While it is impossible to compare our simulations with a subsurface ocean directly to observations of depths and diameters, our results show that when craters are large enough compared to the depth to the ocean, the ocean dramatically modifies the cratering process. Thus, our results generally support Schenk's interpretation of the craters on the Galilean satellites.

4.2 Hot Plugs and Central Pits on Icy Satellites

Craters with small, rimmed or rimless central depressions (central pit craters) are common on both Ganymede and Callisto (Figure 9). On Ganymede, central pit craters are seen from about 5 to 100 km in diameter (Alzate and Barlow, 2011), and are the dominant crater morphology for craters from about 35 to 60 km in diameter (Schenk et al., 2004). Proposed models for central pit formation generally invoke the actions of ice and/or liquid water during the cratering process. Croft (1981; 1983) suggested that central pits form when the central peak has a large fraction of liquid, which drains away and causes the peak to collapse into a pit. Passey and Shoemaker (1982) hypothesized that ice is too

weak to support the weight of large central peaks; thus the peak collapses under its own weight and forms a central pit. Wood et al. (1978) attributed central pits to explosive decompression as ice volatilizes during the impact. Finally, central pits have also been explained as the result of impact into compositionally or rheologically distinct layers at depth (Greeley et al., 1982; Schenk, 1993).

Previously suggested hypotheses for central pit formation lacked quantitative measures to compare to observations. Here, we investigate the possibility that central pits are related to the presence of the hot (>270 K) plug that forms during impact cratering in ice. First, we consider the spatial scale of the hot plug feature. There are two potential ways to measure the width of the hot plug: either by measuring the width that extends to depth (labeled A in Figure 3C; results shown in Figure 10A) or by measuring the extent at the surface (labeled B in Figure 3C; results shown in Figure 10B). We find that the ratio of hot plug diameter to crater diameter predicted by the simulations is in good agreement with measurements of the ratio of central pit diameter to crater diameter (Figure 10). Measurements using the first method (Figure 10A) are well within the range of pit diameter to crater diameter ratios (0.11-0.38) for Ganymede, and cluster around the median of 0.19 for craters greater than about 20 km (Alzate and Barlow, 2011). Note that Alzate and Barlow (2011) observe no regional or latitudinal trends in central pit diameter. Schenk's (1993) measurements of pit diameter to crater diameter are also concentrated around 0.2 for crater diameters between about 40 and 70 km and extend up to 0.4 and 0.5 for larger craters (120-150 km) on Callisto and Ganymede, respectively. Note that the ratios of the width of the hot plug at the surface to the crater diameter (Figure 10B) are higher than the observed ratios for central pits, and we do not favor comparison between this hot thin layer (see Figure 2E) and central pits. The observed depth of central pits is about 1 km (Bray et al., 2009; Schenk, 1993); if their formation involves draining of liquid water, then the thin layer of hot material, itself about 1 km thick, may have insufficient mass as it is a mixture of melt and ice. Also, we note that the modeled pit to crater diameter may vary slightly with the thermal gradient (and hence, with time); however, we leave this topic for future work.

Second, we compare the simulation results to the observed size range of craters with central pits. In the simulations, the mass of the hot plug within craters decreases as a power law with decreasing crater diameter (Figure 5). As a result, the ratio of the plug width to crater diameter is significantly smaller for craters less than about 20 km compared to larger craters (Figure 10). If the hot plug is related to central pits, then the smaller width of the plug for craters less than 20 km is consistent with the observations that central pits are not abundant in smaller craters.

Third, we address the question of why central pit craters sometimes appear near central peak craters of a similar preservational state (a proxy for age) and size (Alzate and Barlow, 2011). This observation suggests that the target properties are not likely to solely control central pit formation. If hot plugs are genetically related to central pits, the variability in crater morphologies may result from differences in impactor velocities. In addition to the total impact energy, the mass of the hot plug is sensitive to the impact velocity, as shown in Figure 11. For these simulations, the size of the impactor was varied so that the total kinetic energy was constant; thus, all of the simulations produce similar final crater diameters (for the 15 km/s impact, the projectile was 2 km in diameter, giving final crater diameters of 39.0 and 46.5 km for the cold and warm cases, respectively). At low impact velocities (< 5 km/s), the mass of the hot plug drops off dramatically to zero. The formation of hot material by an impact is dependent on the amplitude of the shock pressures and the initial temperature (Stewart et al., 2008). The mass of the hot plug also drops off gradually at very high velocities. In this case, more of the highly shocked material is vaporized rather than melted, and the shock pressures decay more steeply with distance from the impact compared to slower velocities. The velocity dependence for the formation of hot plug material is an example of where the assumption of pure energy scaling in crater formation processes breaks down. Thus, if two adjacent craters of similar age and size have different interior morphologies, then the one without a central pit may have been created by either a very low

speed or very high speed impact (relative to the average impact velocity on Ganymede). Note that low impact velocities (<5 km/s) may be achieved by planetocentric secondary impacts, but are unlikely to form craters greater than about 20 km in diameter (Alvarellos et al., 2002). However, comets impact Ganymede at velocities from several km/s to about 30 km/s (Jupiter family comets) and 40 km/s (isotropic comets) (Zahnle et al., 1998). A difference in impact velocity from 10 km/s to 40 km/s can halve the mass of the hot plug (Figure 11).

Fourth, there are a series of interesting observations concerning the rimwall structure of central pit craters. The terrace zone of these craters is much less extensive than expected from comparison to similarly-sized lunar craters: the number of terraces is less (one terrace versus several for lunar craters), the rimwall widths are narrower, and the rim heights increase more steeply with diameter (Schenk, 1993). Thus the evidence suggests that a mechanism is at work to limit the amount of rimwall failure (Schenk, 1993). During crater formation on a rocky body, the collapsing walls of the crater collide with each other (or the central peak) when they reach the crater center, and this collision limits the amount of rim failure. However, during crater formation in ice, the collapsing walls of the crater collide not with each other, but with the slow-moving central plug. Thus, we speculate that the central plug may act to impede collapse and limit the amount of rimwall failure. This interesting possibility should be investigated in future work.

Finally, central pits are a common feature on Ganymede and Callisto rather than on rocky, relatively ice-free bodies like the moon. The formation of the hot plug is directly related to the peculiarities of H₂O and would not be expected on rocky planets. We address the issue of why central pits are found only on certain icy satellites in the next section. The dependence of the hot plug diameter on the crater collapse parameters is discussed in section 4.4.

Our results strongly suggest that central pit formation is related to the formation of the hot plug. Because central dome craters are transitional to central pit craters (i.e., both lie on the same depth versus diameter line, with interior morphologies transitioning from pits to domes with increasing crater diameter, and central domes are surrounded by a ridge that is believed to be equivalent to central pit rims), it is likely that the evolution of the hot plug transitions from central pits to central domes at larger diameters (Schenk, 1993). Perhaps this transition is related to the greater fractions of liquid in the hot plug for larger craters. However, the development of the hot plug into a central pit or dome is beyond the scope of this work. As mentioned in previous hypotheses (Croft, 1981), the fact that melt will drain into fractures in the crater floor (a process not modeled in the simulations) may contribute to formation of the pit. Note that Schenk (1993) argued against a liquid water origin for central domes based on the observations that melt lines the crater floor on rocky bodies and that the dome volumes are too large to be refrozen melt. Here we have shown that the unique excavation processes in ice cause the most highly shocked material to be concentrated in a plug at the crater center, instead of lining the crater floor.

4.3 Central Pits on Other Solar System Bodies

To date, amongst the icy satellites, only Ganymede and Callisto have definitive observations of central pit crater morphologies. Craters on Europa lack central pits, with the morphologies transitioning directly from central peaks to anomalous forms (Figure 1). The onset of anomalous forms at smaller diameters has been suggested to be related to the thinner ice shell on Europa compared to Ganymede and Callisto (Schenk, 2002). By the time craters are large enough to form central pits on Europa, crater formation is instead influenced by the presence of a subsurface ocean (Schenk and Turtle, 2009).

While the gravity on the largest Saturnian moon Titan (1.35 m/s^2) is similar to the gravity on Ganymede and Callisto, the surface of Titan is actively eroded and preserves very few impact craters (Wood et al., 2010), making it difficult to discern if central pits had formed. The smaller Jovian and Saturnian icy satellites lack craters with definitive central pits, although there are a few possible candidate craters (Schenk, 1993). These candidates show that the onset of central pit morphologies

occurs with larger craters on smaller bodies, however the onset does not scale perfectly inversely with gravity (Chapman and McKinnon, 1986; Schenk, 1993). The largest craters on several satellites could have central pit morphologies using simple gravity scaling from Ganymede and Callisto, but instead the craters show central peaks (Chapman and McKinnon, 1986). For example Triton's (0.78 m/s^2 ; Triton is a moon of Neptune and the largest moon beyond Saturn) largest crater is 25 km in diameter. This diameter is larger than a gravity-scaled central pit transition of about 16 km, and yet the crater does not exhibit a central pit.

If the formation of central pits is related to the volume of shock-generated melt, as in the model suggested here, then the onset of central pit morphologies should occur with larger craters on smaller icy satellites (because it takes less energy to create a crater of the same size on a smaller body than on a larger body), as observed. However, the formation of pits will not scale perfectly with gravity. As illustrated in Figure 11, the mass of the hot plug is a function of not only the impact energy, but the velocity as well (which determines the peak shock pressure). The dependence on velocity will prevent perfect gravity scaling.

While there are as of yet no observations of craters on Pluto, we predict that no central pit craters should exist as a result of the low gravity (0.64 m/s^2) and low impact velocities (average of 1.9 km/s (Zahnle et al., 2003)). An observation of large craters on Pluto without central pits (greater than about 60 km diameter by pure gravity scaling from Transition II) would be strong support for a velocity/pressure-dependence for the genesis of central pits. Finally, central pits are also observed in craters on Mars (Barlow, 2006; Barlow, 2007; Barlow, 2009; DeVries and Barlow, 2009; Wood et al., 1978). Unlike the central pits on Ganymede, the Martian pits are observed not only in the bottom of craters, but on the top of central peaks as well. Hence, the formation of Martian pits may or may not be analogous to pits on icy satellites. Hypotheses for Martian pit formation generally involve the presence of subsurface ice rich layers (Barlow, 2006; Barlow, 2007; Barlow, 2009; DeVries and Barlow, 2009; Wood et al., 1978).

4.4 Limitations and Assumptions

In this work, we have focused on aspects of impact crater formation that are unique to high energy impacts onto icy surfaces. The results presented here are principally dependent upon the accuracy of the equation of state model for H_2O and the crater collapse process.

Equation of State

As discussed in section 2, the equation of state model includes five phases. In particular, the ice Ih boundary with ice VI is artificial. The original justification for this simplification in the phase diagram is based on shock wave experiments (Stewart and Ahrens, 2005). The dynamic strength of ice Ih is larger than the phase space between ice Ih and VI. Hence, the first phase transformation on the ice shock Hugoniot is to ice VI, skipping the intermediate phases (ices III, V, and II). The second and third transitions are to ice VII and supercritical fluid, respectively. The uncertainty in the model equation of state primarily arises during the decompression of ice VI and ice VII.

Ices VI and VII may decompress metastably to ambient pressures at sufficiently low temperatures (e.g., cooled to 77 K by liquid nitrogen). However, upon heating, ice VI and ice VII will transform to ice Ic (and then later to ice Ih) at about 150 and 120 K, respectively (Bertie et al., 1964). Thus, because shock compression is accompanied by irreversible heating and the initial temperatures in this work were at or above 120 K, we expect the high pressure solid phases to transform back to ice Ih upon decompression. The uncertainty lies in where along the decompression path the transformation takes place. In the equilibrium model, the transformation back to ice Ih occurs at the model phase boundary. In reality, the transformation probably occurs at pressures below the phase boundary because of phase change kinetics. At present, we are unable to model the kinetics of delayed transformations between phases. In the case of ice, it would appear that the equilibrium phase boundaries for ice VI and VII are applicable during shock compression (Stewart and Ahrens, 2005), but

that kinetically modified boundaries are more appropriate upon release. Unfortunately, no shock decompression data exist that could define the parameters for a kinetic model.

We investigated the sensitivity of hot plug formation to the pressure of the artificial phase boundary between ice Ih and VI. In the nominal phase diagram, the ice Ih-VI boundary is at the actual ice Ih-II and ice Ih-III boundaries, near 200 MPa. In other words, the phase space of ice VI has been extended. For comparison, we constructed a model equation of state with the ice Ih-VI boundary at the actual ice VI phase boundary, near 632 MPa. In this case, the phase space of ice Ih has been extended. Changing the boundary slightly modifies the excavation flow field but does not change the phenomenon of discontinuous excavation. Raising the boundary decreases the amount of central plug material but does not significantly change final crater shape or the amount of hot material within the plug: for a 120 K isothermal target with a 2 km diameter impactor, the hot plug mass was 2.5×10^{14} kg with the 200 MPa boundary and 2.8×10^{14} kg with the 632 MPa boundary. Similarly, lowering the phase boundary to 50 MPa (to simulate delayed decompression) also does not change the phenomena of discontinuous excavation. Note that most of the material within the hot plug was shocked to pressures greater than ~ 2 GPa (the criteria for incipient melting (Stewart et al., 2008)); hence, the exact location of the ice Ih-ice VI boundary (at lower pressures) is not significant.

The phenomenon of discontinuous excavation arises because of the creation of the high-pressure ice phases during shock compression, which has been shown experimentally. The exact volume of high-pressure material depends on the details of the model phase boundary but does not vary significantly for the approximations described here. We conclude that the phenomenon of discontinuous excavation is not an artifact of the model equation of state. It is a robust feature based on the characteristics of H₂O (see Appendix).

Finally, coexistence of two phases, such as solid and vapor, is described by an average state (e.g., average density and internal energies) in the tabular EOS. The two phases are treated as a single material. In other words, there is no separation of the phases that could lead to two-phase flow, and the vapor is not allowed to diverge from the solid. The late stage evolution of the hot plug would be more realistically described by a model that allowed for two-phase flow.

Crater Collapse

The depths versus diameters of the simulated craters do not *exactly* match the observations (Figure 6): the simulated simple craters are slightly shallow and the complex craters are slightly deeper than observed. The final crater shape is dependent on both the quasi-static strength model and the crater collapse model. Although the quasi-static strength model is fit to laboratory data, it may not precisely represent an icy planetary crust. Our simulations also assumed a perfectly intact surface (e.g., no initial fractures).

As discussed in section 2, the choice of acoustic fluidization parameters in the crater collapse model is uncertain. The acoustic fluidization model is tunable enough so that, if desired, parameters may be chosen such that simulated craters reproduce the mean observations (Bray et al., 2008) (regardless of the thermal gradient). However, this approach would obscure the physics behind what is controlling the observed crater morphologies. Instead, we chose to fix the parameters that control the cratering mechanics (equation of state and strength models) and to vary other parameters: the impact conditions and target properties. In Figure 6, because the cratering mechanics model for the two sets of simulations is identical, we attribute the observed variation (the transition from increasing depth with diameter to decreasing depth with diameter at 30 km) to be the result of the different initial thermal profiles. The implicit assumption behind this approach is that the same cratering mechanics model applies over the entire size range of craters studied here.

We also considered the sensitivity of the geometry of the hot plug to the acoustic fluidization parameters (primarily the effective viscosity and decay time scale). While the mass of the hot plug is independent of the acoustic fluidization parameters, the final configuration of the plug is not. For

example, if the acoustic fluidization viscosity is raised (less collapse), then the plug will undergo less squeezing during collapse, and the final crater diameter will be smaller. Thus, the ratio of liquid plug diameter to crater diameter will increase. If the acoustic fluidization viscosity is lowered (more collapse), then the plug will undergo more squeezing during collapse (becoming thinner), and the final crater diameter will be larger. Thus, the ratio of liquid plug diameter to crater diameter will decrease. For the 2-km diameter projectile simulation (Figure 2), the ratio of hot plug diameter to crater diameter (using measurement method A) was 0.18 (Figure 10). Adjusting the acoustic fluidization viscosity by one order of magnitude above and below the nominal value changes the plug to crater diameter ratio to 0.24 and 0.10, respectively. These values are still consistent with the range of values (0.11 to 0.3) measured by Alzate and Barlow (2011) and Schenk (1993). While this is compelling support for a relationship between plugs and central pits, we have not modeled the evolution of the plug into a central pit or dome. The shock code cannot model the necessary processes, and this important step is left for future work. Variations of the decay time scale (from one half to double the nominal value) also did not induce significant morphological changes in the hot plug. Over the range of acoustic fluidization parameters that produce final crater depth to diameters in the observed range, the hot plug morphologies are similar and the results presented in Figure 10 are robust.

Composition

In this work, the composition of the projectile and target was pure H₂O ice. The addition of significant amounts of other materials (both other volatiles and refractory phases) will affect both the equation of state and the strength model. If the target is predominantly H₂O ice, then we expect the rheology to be dominated by ice. Similarly, discontinuous excavation should be present in a surface primarily composed of H₂O ice. Hence, the results presented here should be widely applicable to icy satellites.

2D versus 3D

The calculations in this work were all conducted using two-dimensional cylindrical geometries and thus suffered from artifacts along the $x=0$ symmetry boundary condition. A few low resolution 3D calculations were conducted to explore the effect of the calculation geometry and impact angle (see online supplemental information). The mass and spatial distribution of the hot plug (>270 K) was quantitatively similar in the 2D and 3D cases (Table S1). However, the amount of completely melted material (>273.5 K) decreased in 3D. In the 2D calculations, much of the completely melted material (the very high red and yellow colored temperatures along the center line of Figure 2E) is an artifact of the centerline boundary. Additionally, two dimensional calculations may only consider vertical impacts. Discontinuous excavation is also observed in our 3D oblique impact calculations (animations available in the online supplemental information). Although the spatial distribution of shock pressures close to the impact site is strongly affected by the impact angle, the shock pressure field at distances 2-3 times greater than the projectile radius is nearly hemispherical (Kraus and Stewart, 2011; Pierazzo and Melosh, 2000). The low shock pressures (>0.6 GPa) that are required to form the ice polymorphs involved in discontinuous excavation are within the hemispherical zone for the impact velocities discussed here. Hence, the formation of high-pressure polymorphs of ice will produce circular hot plugs for any circular crater formed at the appropriate impact velocity (Figure 11).

5. Conclusions

In this work, we simulated crater formation on the icy satellite Ganymede using recent improvements in the models for the equation of state and strength of H₂O ice. In particular, the model equation of state includes the dense high-pressure ice polymorphs ices VI and VII. We find that the shock-induced formation of these polymorphs leads to a phenomenon we call discontinuous excavation, whereby a gap is created in the excavation flow. Over a certain range of impact energy and impact

velocity, the highly-shocked material that is interior to the discontinuity is concentrated in a hot, partially liquid plug in the crater floor during crater collapse.

We examined the possibility that the hot plug may be genetically related to observed central pits. Several observations support this proposed origin for central pits. First, the calculated geometries of hot plugs are similar to observed ratios of pit width to crater diameter. Second, the range of crater sizes that are dominated by central pit morphologies overlaps with calculations of when a substantial hot plug of material will form in a crater floor. Third, variations in the morphology of craters of similar size (with and without central pits) can be explained by differences in impact velocity. Fourth, decreased amounts of rim collapse may be explained by the central plug impeding collapse. Finally, the occurrence of central pits on only the largest icy satellites (without active resurfacing) is related to the impact energy and velocities required to create a sufficient mass of hot material.

Our simulations explored the effect of varying the impact conditions and target thermal gradient on impact crater formation on icy satellites. By using independently derived model parameters (quasi-static strength parameters determined by laboratory experiments, acoustic fluidization parameters fitted to lunar data, and an equation of state based on laboratory data), we can illustrate a diversity of cratering phenomena, including the discovery of discontinuous excavation and hot plug formation. In a demonstration of the reliability of the independent model input parameters, the geometry (depth and diameter) of simulated craters are in good agreement with observations.

The simulated craters also provide some insight into the observed transition in crater depths with increasing diameters on the icy Galilean satellites. The calculated crater depths begin to decrease with increasing crater diameter above about 30 km when the target has a warm thermal gradient, whereas crater depths continue to increase in a cold isothermal crust. The warm thermal gradient calculations are in good agreement with observations on Ganymede and Callisto and support the suggestion by Schenk (2002) that the transition in crater geometries is related to a rheological transition within the icy satellites. Our simulations also qualitatively support the interpretation that the dramatic decrease in depth for the largest craters on the icy Galilean satellites is related to the presence of a subsurface ocean (Schenk, 2002; Schenk and Turtle, 2009).

Appendix

The 5-Phase Model Equation of State for H₂O

The tabular 5-phase model equation of state was developed to capture the phase changes observed on the experimental ice Hugoniot (Stewart and Ahrens, 2005). The methodology used to construct the EOS table is described in the appendix in Senft and Stewart (2008). The model is compared to experimental boundaries for the known stable phases in Figure A1. Recent measurements of the melting curve of ice VII (summarized in Dunaeva et al., 2010) are scattered and generally slightly higher than the model; however, the high-pressure portion of the ice VII melting curve does not impact the results presented here. The tabular equation of state is available from Stewart.

Discontinuous Excavation

The phenomenon of discontinuous excavation arises because of the shock-induced formation of ices VI and VII and the back transformation to ice Ih. We confirmed that the observed phenomenology during impact cratering simulations was robust by using a simple phase transformation equation of state model (ptran in CTH). The test equation of state was composed of two Mie-Grüneisen segments that represented ice Ih and a dense, high-pressure phase. The high-pressure phase transformed back to the low-pressure phase upon unloading. As with the 5-Phase H₂O equation of state, a gap developed during crater excavation at the location of the onset of the high-pressure phase.

Five segments are observed on the H₂O ice Hugoniot: ice Ih (elastic), ice Ih (shock), ice VI, ice VII, and supercritical fluid (Stewart and Ahrens, 2005). The loading and release paths are dramatically different between the (1) ice Ih, (2) ices VI and VII, and (3) supercritical fluid regions. These paths are shown schematically in Figure A2 (for data points refer to Figure 15 in Stewart and Ahrens, 2005). Within the ice Ih region, the loading and unloading paths approximately follow the Hugoniot. In the ices VI and VII region, the loading path involves a significant volume compression and the release path is steep until the transformation to ice Ih (dotted line). In contrast, ice shocked to supercritical fluid releases along a shallower path (dashed line).

In the decaying shock front during an impact event, material shocked to the supercritical fluid phase boundary at around 6 GPa is adjacent to material shocked to ice VII. Although the two parcels of material have continuous particle velocities in their peak shock states, upon release their particle velocities will diverge because of the difference in release paths. A similar process will occur at the ice Ih-ice VI transition. More generally, material is accelerated to a particle velocity, $u_{p,H}$, by the shock wave. Upon arrival of the rarefaction wave with particle velocity $u_{p,R}$, the particle velocities sum,

$$u_p = u_{p,H} \pm u_{p,R}, \quad (1)$$

where the sign depends on the direction of the rarefaction wave. The values add when the rarefaction wave direction is opposite the shock wave (e.g., in a laboratory measurement of downrange free surface velocities) and subtract when the wave directions are the same, as during impact cratering. The particle velocity contribution from the isentropic rarefaction wave is given by the Riemann integral (e.g., Rice et al., 1958),

$$u_{p,R} = \int_{P_R}^{P_H} \left(-\frac{dV}{dP} \right)_S^{1/2} dP = \int_{P_R}^{P_H} \frac{V dP}{c_R}, \quad (2)$$

where c_R is the bulk sound speed (the rarefaction wave velocity), P is pressure, V is specific volume, and S denotes isentropic release. The subscripts H and R refer to the Hugoniot and release states, respectively. Note that the slope of the release path is related to the sound speed in the shocked state; hence the steeper release from ices VI and VII reflects the larger sound speed of these phases.

From Equation (2) and the release paths in Figure A2, the release wave particle velocity of material shocked to point A and fully released will be larger than for material shocked to point B and released to point B', which in the simulations corresponds to the ice Ih-ice VI phase boundary. Recall

that the back transformation to ice Ih is delayed during impact cratering until the volume increase may be accommodated by the excavation flow. Depending on the geometry of the problem, a gap may form initially between material released completely from the supercritical state (point A) and material released to point B'. When the transformation from ice VI to ice Ih is finally achieved, the velocity of the parcel of material released from point B' is significantly changed. Similarly, material shocked to points C and D will have continuous particle velocities in the shock state and very different particle velocities upon release. In the geometry of an impact cratering event, the annulus of material shocked to ices VI and VII obtains fully released particle velocities sufficiently slower to result in separation of the annulus from material shocked to ice Ih (point D). Hence, materials shocked to ice VI and VII are incorporated into the central plug during discontinuous excavation.

The previous discussion focused on a single shock and single release wave. Note that the impedance (density \times sound speed) contrast between ices VI and VII and the surrounding phases leads to partial reflections of the rarefaction wave, which forms the tail of the detached (hemispherical shell) shock. The reflecting waves also act to slow down the material in the central plug; however, the back transformation from ice VI to ice Ih provides the greatest disruption to the excavation flow.

To illustrate the formation of a gap from the processes described above, we consider a simple impact geometry: a thin plate impacting a half space. We simulated a one-dimensional impact by a 3-mm sheet of ice onto a half space of ice at 15 km/s. An animation of this event is available in the online supplemental materials.

References

- Alvarellos, J. L., Zahnle, K. J., Dobrovolskis, A. R., Hamill, P., 2002. Orbital evolution of impact ejecta from Ganymede. *Icarus*. 160, 108-123.
- Alzate, N., Barlow, N. G., 2011. Central pit craters on Ganymede. *Icarus*. 211, 1274-1283.
- Artemieva, N., Lunine, J., 2003. Cratering on Titan: impact melt, ejecta, and the fate of surface organics. *Icarus*. 164, 471-480.
- Artemieva, N., Lunine, J., 2005. Impact cratering on Titan II. Global melt, escaping ejecta, and aqueous alteration of surface organics. *Icarus*. 175, 522-533.
- Barlow, N. G., 2006. Impact craters in the northern hemisphere of Mars: Layered ejecta and central pit characteristics. *Meteoritics & Planetary Science*. 41, 1425-1436.
- Barlow, N. G., 2007. Central pit craters on Mars and Ganymede. *Meteoritics and Planetary Science Supplement*. 42, 5120.
- Barlow, N. G., 2009. Martian central pit craters: summary of northern hemisphere results. *Lunar Planet. Sci. XL. Abstract 1915*.
- Bertie, J. E., Whalley, E., Calvert, L. D., 1964. Transformations of ice VI and ice VII at atmospheric pressure. *Canadian J. Chem.* 42, 1373-1378.
- Billings, S. E., Kattenhorn, S. A., 2005. The great thickness debate: Ice shell thickness models for Europa and comparisons with estimates based on flexure at ridges. *Icarus*. 177, 397-412.
- Bray, V. J., Collins, G. S., Morgan, J. V., Schenk, P. M., 2008. The effect of target properties on crater morphology: comparison of central peak craters on the Moon and Ganymede. *Meteoritics & Planetary Science*. 43, 1979-1992.
- Bray, V. J., Schenk, P. M., Melosh, H. J., Collins, G. S., Morgan, J. V., 2009. Dimensions of central pits in Ganymede craters. *Lunar Planet. Sci. XL. Abstract 1350*.
- Chapman, C. R., McKinnon, W. B., Cratering of Planetary Satellites. In: J. A. Burns, M. S. Matthews, (Eds.), *Satellites*. University of Arizona, 1986, pp. 492-580.
- Chyba, C., 2000. Energy for microbial life on Europa. *Nature*. 403, 381-382.
- Collins, G., Numerical Modeling of Large Impact Crater Collapse. Department of Earth Science and Engineering, Vol. Ph.D. University of London, 2002, pp. 235.
- Collins, G. S., Melosh, H. J., Ivanov, B. A., 2004. Modeling damage and deformation in impact simulations. *Meteoritics & Planetary Science*. 39, 217-231.
- Crawford, D. A., Adaptive mesh refinement in CTH. Technical Report SAND99-1118C. Sandia National Laboratories, Albuquerque, NM, 1999, pp. 10.
- Croft, S. K., 1981. On the origin of pit craters. *Lunar Planet. Sci. XII. Abstract p. 196-198*.
- Croft, S. K., 1983. A proposed origin for palimpsests and anomalous pit craters on Ganymede and Callisto. *Proc. Lunar Planet. Sci. Conf 14th. p. 71-89*.
- DeVries, R. J., Barlow, N. G., 2009. Central pit craters in the southern hemisphere of Mars. *Lunar Planet. Sci. XL. Abstract 1929*.
- Dombard, A. J., McKinnon, W. B., 2000. Long-term retention of impact crater topography on Ganymede. *Geophysical Research Letters*. 27, 3663-3666.
- Dunaeva, A. N., Antsyshkin, D. V., Kuskov, O. L., 2010. Phase Diagram of H₂O: Thermodynamic Functions of the Phase Transitions of High-Pressure Ices. *Solar System Research*. 44, 202-222.
- Feistel, R., Wagner, W., 2007. Sublimation pressure and sublimation enthalpy of H₂O ice Ih between 0 and 273.16 K. *Geochimica et Cosmochimica Acta*. 71, 36-45.
- Golombek, M. P., Banerdt, W. B., 1986. Early thermal profiles and lithospheric strength of Ganymede from extensional tectonic features. *Icarus*. 68, 252-265.
- Greeley, R., Find, J. H., Gault, D. E., Guest, J. E., Impact cratering on icy satellites. In: D. Morrison, (Ed.), *Satellites of Jupiter*. University of Arizona Press, Tucson, AZ, 1982, pp. 340-378.

- Kraus, R. G., Stewart, S. T., 2011. Impacts onto H₂O Ice: Scaling Laws for Melting, Vaporization, Excavation, and Final Crater Size. *Icarus*. submitted.
- Luttrell, K., Sandwell, D., 2006. Strength of the lithosphere of the Galilean satellites. *Icarus*. 183, 159-167.
- McGlaun, J. M., Thompson, S. L., Elrick, M. G., 1990. CTH: a three-dimensional shock wave physics code. *International Journal of Impact Engineering*. 10, 351-360.
- Melosh, H. J., 1979. Acoustic fluidization: a new geologic process? *Journal of Geophysical Research*. 84, 7513-7520.
- Melosh, H. J., Ivanov, B. A., 1999. Impact crater collapse. *Annual Reviews of Earth and Planetary Science*. 27, 385-415.
- Melosh, J., 1989. *Impact cratering: A geologic process*. Oxford University Press, New York.
- Moore, J. M., Malin, M. C., 1988. Dome craters on Ganymede. *Geophysical Research Letters*. 15, 225-228.
- Moore, J. M., et al., 2001. Impact features on Europa: Results of the Galileo Europa Mission (GEM). *Icarus*. 151, 93-111.
- Moore, J. M., Schenk, P. M., Bruesch, L. S., Asphaug, E., McKinnon, W. B., 2004. Large impact features on middle-sized icy satellites. *Icarus*. 171, 421-443.
- Ormo, J., Shuvalov, V. V., Lindstrom, M., 2002. Numerical modeling for target water depth estimation of marine-target impact craters. *Journal of Geophysical Research*. 107, doi:10.1029/2002JE001865.
- Passey, Q. R., Shoemaker, E. M., Craters and basins on Ganymede and Callisto: Morphological indicators of crustal evolution. In: D. Morrison, (Ed.), *Satellites of Jupiter*. University of Arizona Press, Tucson, 1982, pp. 379-434.
- Petrenko, V. F., Whitworth, R. W., 1999. *Physics of ice*. Oxford U., New York.
- Pierazzo, E., Vickery, A. M., Melosh, H. J., 1997. A re-evaluation of impact melt production. *Icarus*. 127, 408-423.
- Pierazzo, E., Melosh, H. J., 2000. Melt production in oblique impacts. *Icarus*. 145, 252-261.
- Pike, R. A., 1976. Crater dimensions from Apollo data and supplemental sources. *Moon*. 15, 463-477.
- Rice, M. H., McQueen, R. G., Walsh, J. M., Compression of solids by strong shock waves. In: F. Seitz, D. Turnbull, Eds.), *Solid State Physics Vol. 6*. Academic Press, New York, 1958, pp. 1-63.
- Schenk, P. M., 1991. Ganymede and Callisto: Complex crater formation and planetary crusts. *Journal of Geophysical Research*. 96, 15635-15664.
- Schenk, P. M., 1993. Central pit and dome craters: exposing the interiors of Ganymede and Callisto. *Journal of Geophysical Research*. 98, 7475-7498.
- Schenk, P. M., 2002. Thickness constraints on the icy shells of the Galilean satellites from a comparison of crater shapes. *Nature*. 417, 419-421.
- Schenk, P. M., Chapman, C. R., Zahnle, K., Moore, J. M., Ages and interiors: the cratering record of the Galilean satellites. In: F. Bagenal, et al., Eds.), *Jupiter: The planet, satellites, and magnetosphere*. Cambridge University Press, Cambridge, UK, 2004, pp. 427-456.
- Schenk, P. M., Turtle, E. P., Europa's Impact Craters: Probes of the Icy Shell. In: R. T. Pappalardo, et al., Eds.), *Europa*. U. Arizona Press, Tucson, 2009, pp. 181-198.
- Schubert, G., Anderson, J. D., Spohn, T., McKinnon, W. B., Interior composition, structure, and dynamics of the Galilean satellites. In: F. Bagenal, et al., Eds.), *Jupiter: The Planet, Satellites, and Magnetosphere*. Cambridge University Press, Cambridge, United Kingdom, 2004, pp. 281-306.
- Senft, L. E., Stewart, S. T., 2007. Modeling impact cratering in layered surfaces. *Journal of Geophysical Research*. 112, doi: 10.1029/2007JE002894.
- Senft, L. E., Stewart, S. T., 2008. Impact crater formation in icy layered terrains on Mars. *Meteoritics and Planetary Science*. 43, 1993-2013.

- Senft, L. E., Stewart, S. T., 2009. Dynamic Fault Weakening and the Formation of Large Impact Craters. *Earth and Planetary Science Letters*. 287, 471-482.
- Showman, A. P., Malhotra, R., 1999. The Galilean satellites. *Science*. 286, 77-84.
- Smith, B. A., et al., 1979. The Galilean Satellites and Jupiter: Voyager 2 Imaging Science Results. *Science*. 206, 927-950.
- Spohn, T., Schubert, G., 2003. Oceans in the icy Galilean satellites of Jupiter? *Icarus*. 161, 456-467.
- Stewart, S. T., Ahrens, T. J., 2005. Shock properties of H₂O Ice. *Journal of Geophysical Research*. 110, doi: 10.1029/2004JE002305.
- Stewart, S. T., Seifert, A., Obst, A. W., 2008. Shocked H₂O ice: Thermal emission measurements and the criteria for phase changes during impact events. *Geophysical Research Letters*. 35, doi: 10.1029/2008GL035947.
- Thompson, S. L., Lauson, H. S., Improvements in the Chart D Radiation-Hydrodynamic CODE III: Revised Analytic Equations of State, Sandia Report #SC-RR-710714. Sandia Laboratories, Albuquerque, NM, 1972.
- Turtle, E. P., Pierazzo, E., 2001. Thickness of a European ice shell from impact crater simulations. *Science*. 294, 1326-1328.
- Turtle, E. P., Ivanov, B. A., 2002. Numerical simulations of impact crater excavation and collapse on Europa: implications for ice thickness. *Lunar Planet. Sci.* XXXIII. Abstract 1929.
- Wagner, W., Pruss, A., 2002. The IAPWS formulation 1995 for the thermodynamic properties of ordinary water substance for general and scientific use. *Journal of Physical and Chemical Reference Data*. 31, 387-535.
- Williams, K. K., Zuber, M. T., 1998. Measurement and analysis of lunar basin depths from Clementine altimetry. *Icarus*. 131, 107-122.
- Wood, C. A., Head, J. W., Cintala, M. J., 1978. Interior morphology of fresh Martian craters: The effects of target characteristics. *Proc. Lunar Planet. Sci. Conf.* 9th. 3691-3709.
- Wood, C. A., et al., 2010. Impact craters on Titan. *Icarus*. 206, 334-344.
- Wünnemann, K., Ivanov, B. A., 2003. Numerical modelling of the impact crater depth-diameter dependence in an acoustically fluidized target. *Planetary and Space Science*. 51, 831-845.
- Zahnle, K., Dones, L., Levison, H., 1998. Cratering rates on the Galilean satellites. *Icarus*. 136, 202-222.
- Zahnle, K., Schenk, P., Levison, H., Dones, L., 2003. Cratering rates in the outer solar system. *Icarus*. 163, 263-289.

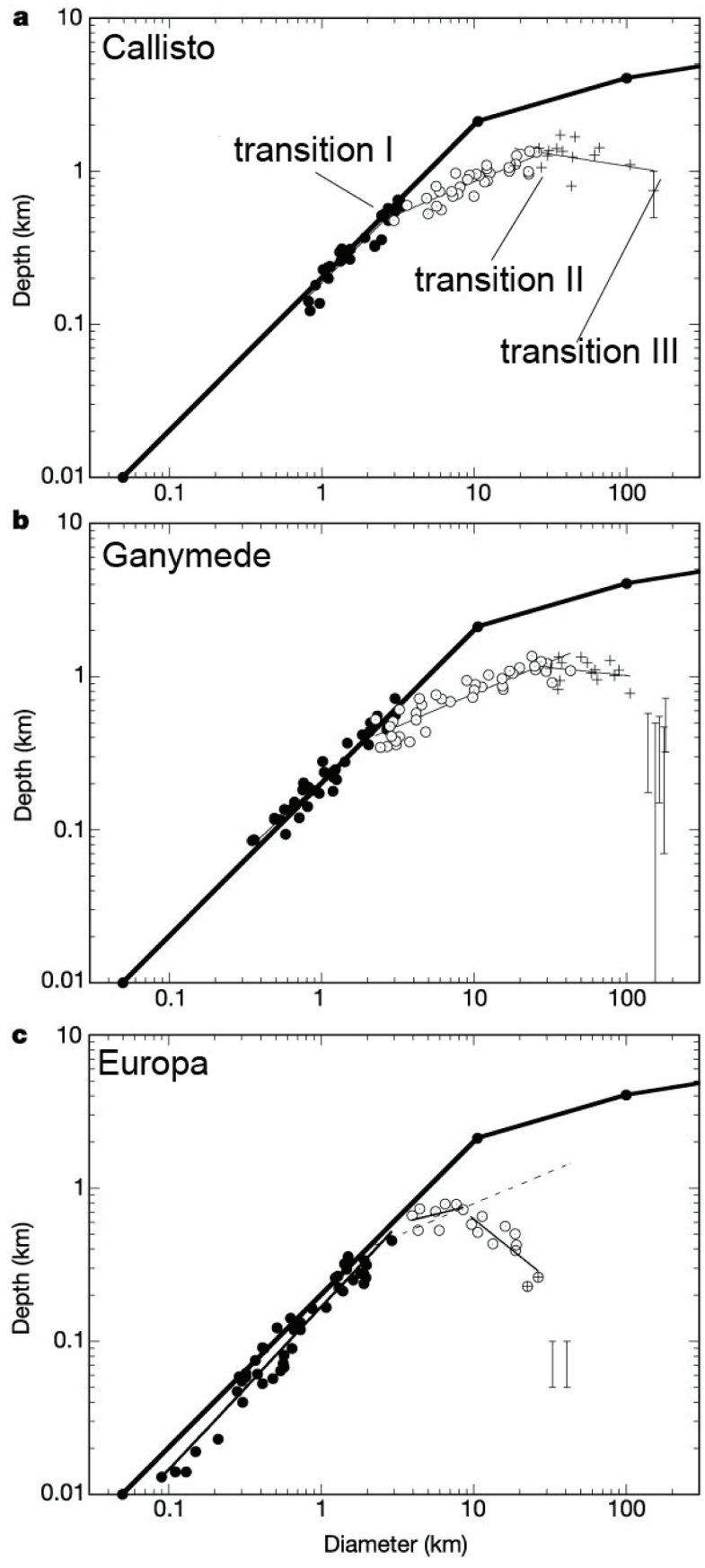


Figure 1: Depth versus diameter measurements for fresh craters on the icy Galilean satellites: Callisto (A), Ganymede (B), and Europa (C). Thick black lines are fits to lunar data, symbols are data points for the icy satellites, and thin lines are fits through the data. The dashed line in C is the Ganymede fit. Simple craters are plotted as solid dots, central peak craters as open circles, central pit and dome craters as crosses, and anomalous forms and multiring basins as error bars. Note that error bar for the one anomalous crater plotted for Callisto is representative of the size of the error bars for the data points where no error bar is plotted. Figure is taken from Schenk (2002). In A, Transitions I and II and III (Schenk's terminology for the observed "kinks" in the depth to diameter data) are identified.

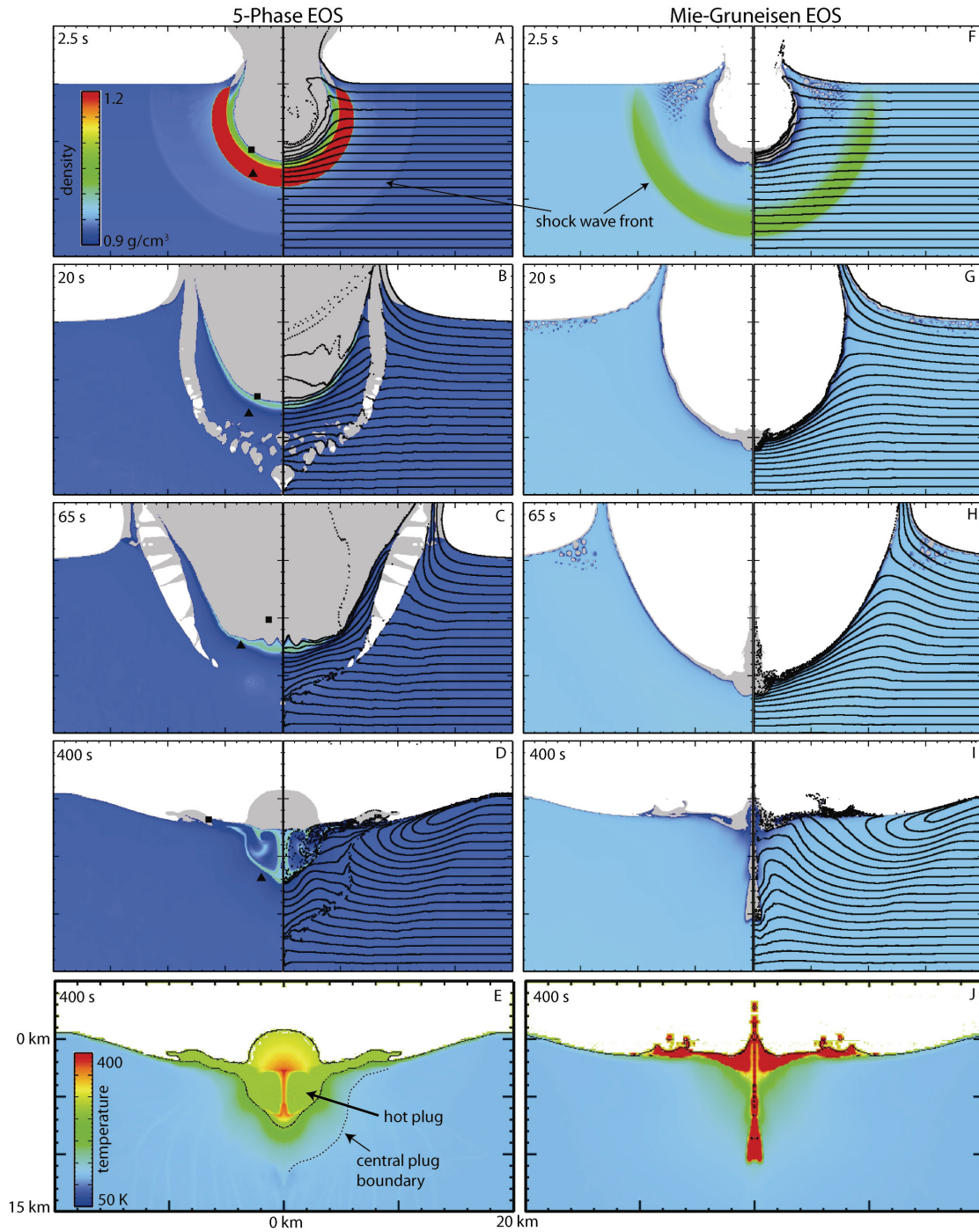


Figure 2: Impact of a 2-km diameter projectile onto a 120-K isothermal Ganymede at 15 km/s using the 5-Phase EOS (A-E) and the Mie-Grüneisen EOS (no phase changes) for ice Ih (F-J). A-D and F-I show density at different times during crater formation, and the black dots are initially horizontal rows of Lagrangian tracer particles. Gray material is partially/fully vapor with densities between 0.0001 and 0.9 g/cm³. In A-D, ice Ih is indicated by dark blue, ices VI and VII as red, and liquid water as light blue and green. Triangle and square points correspond to data in Figure 4A and B, respectively. E and J show temperature at 400 s; temperatures in J are unreliable. Also, the high temperatures (colored red and

yellow) along the centerline of E are an artifact due to the symmetry boundary condition. The black line in E is the 270 K contour (hot plug), and the dashed line shows the central plug boundary (on one side). Spatial, density, and temperature scales are the same both columns. Final craters are about 40 km in diameter. See supplemental material for animations.

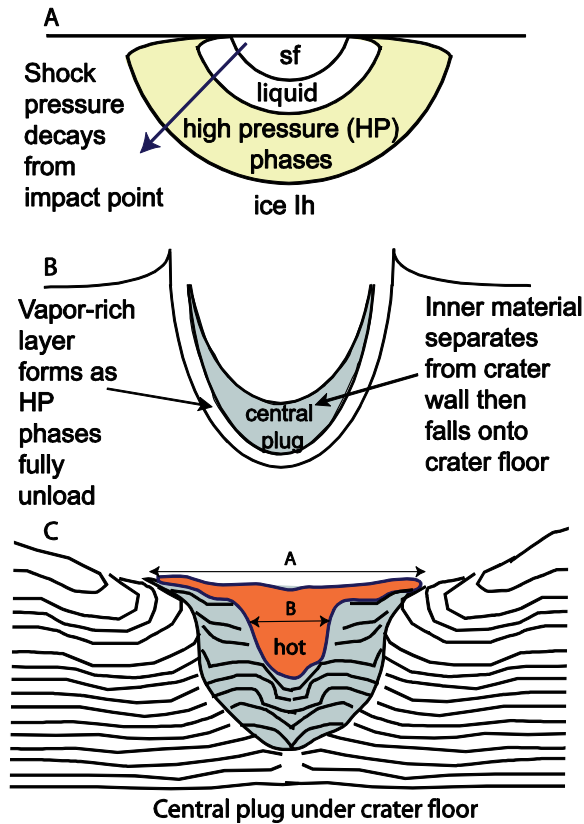


Figure 3: Schematic of an impact cratering event on an icy satellite analogous to the simulation shown in Figure 2A. Panels do not have the same scale. (A) Initial locations of material undergoing shock-induced phase changes (sf is supercritical fluid; high pressure phases are ices VI and VII). (B) The impedance mismatch between the high-pressure phases and lower density phases (liquid above and ice Ih below) leads to a discontinuity in the crater excavation flow. The rarefaction wave only partially decompresses the high-pressure phases (to the phase boundary); complete decompression is achieved when the excavation flow allows for the volume expansion into ice Ih. The material at the discontinuity releases to the ice Ih-vapor boundary. (C) During crater collapse, the most highly shocked material is concentrated and compressed in a central plug defined by a stratigraphic discontinuity (colored in gray) in the crater floor. A hot plug of material (>270 K) is concentrated within the central plug.

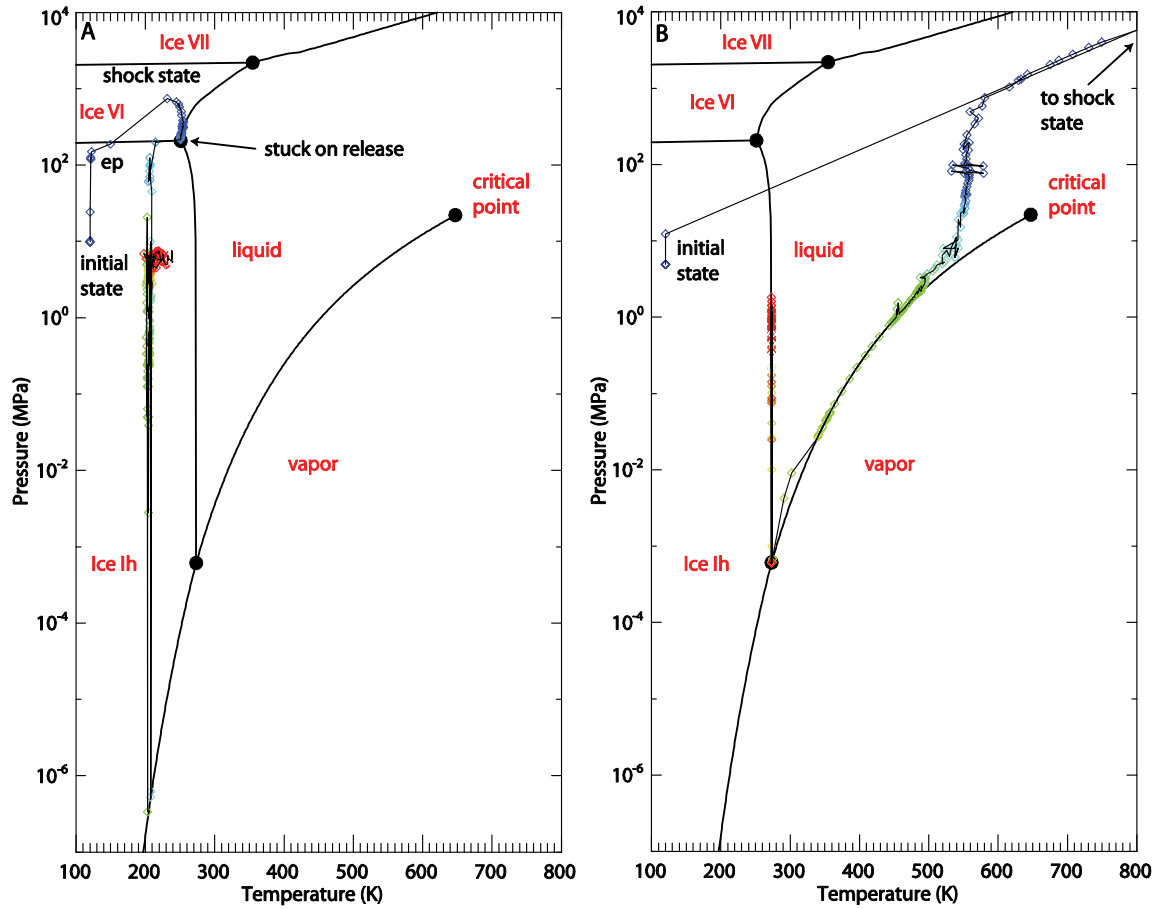


Figure 4: Example Lagrangian tracer paths (colored points) from simulation shown in Figure 2A plotted on the simplified H₂O phase diagram of the 5-Phase EOS. Symbol colors indicate time from 0 s (purple) to 180 s (red). A. The material is shocked first to the elastic precursor state (ep) and then to 0.74 GPa, releases to the ice VI/liquid boundary and down to the Ice VI/liquid/ice Ih triple point, where it remains at the triple point until expansion into ice Ih can be accommodated by the excavation flow, after which it continues decompressing to the ice Ih/vapor boundary. The material is slightly pressurized during crater collapse. Initial location was $x = 2.38$ km, $y = -7.5$ km, and location at 400 s was $x = 1.9$ km, $y = -6.95$ km (triangle point in Fig. 2A-D). B. The material was shocked to 11.15 GPa, released to the saturation vapor curve and down to the triple point. The material was pressurized along the melting curve during crater collapse. Initial location was $x = 1.38$ km, $y = -3.75$ km, and location at 400 s was $x = 6.48$ km, $y = -1.89$ km (square point in Fig. 2A-D).

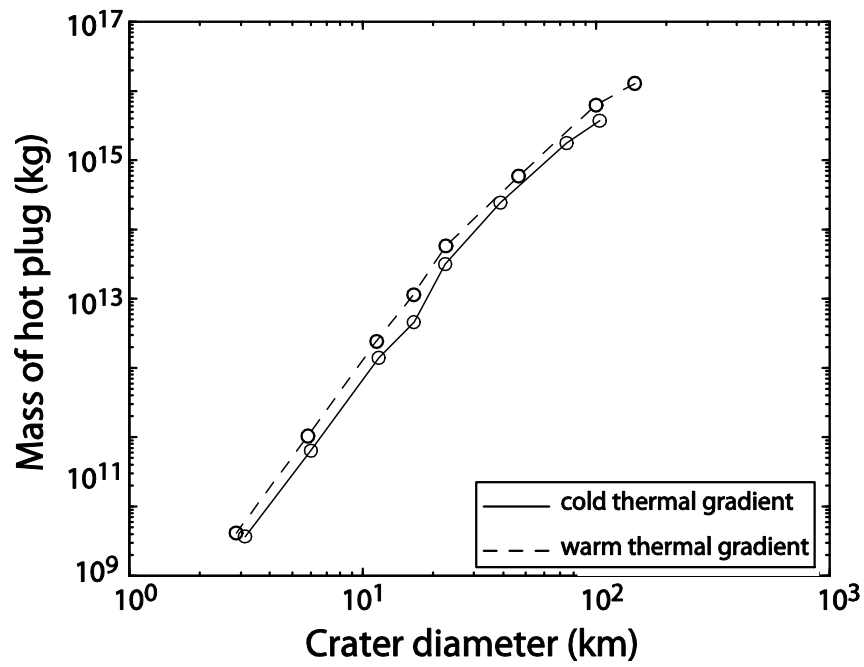


Figure 5: Mass of hot plug versus crater diameter for a cold and a warm thermal profile. The volume of the hot plug is defined by the 270 K temperature contour (thin lines) and represents partial melt. Power law fits for the 270 K contour masses are as follows: $m = 10^{7.75} D^{4.03}$ for the cold case, and $m = 10^{8.20} D^{3.83}$ for the warm case (m is the mass of the hot plug in kg and D is the diameter in km).

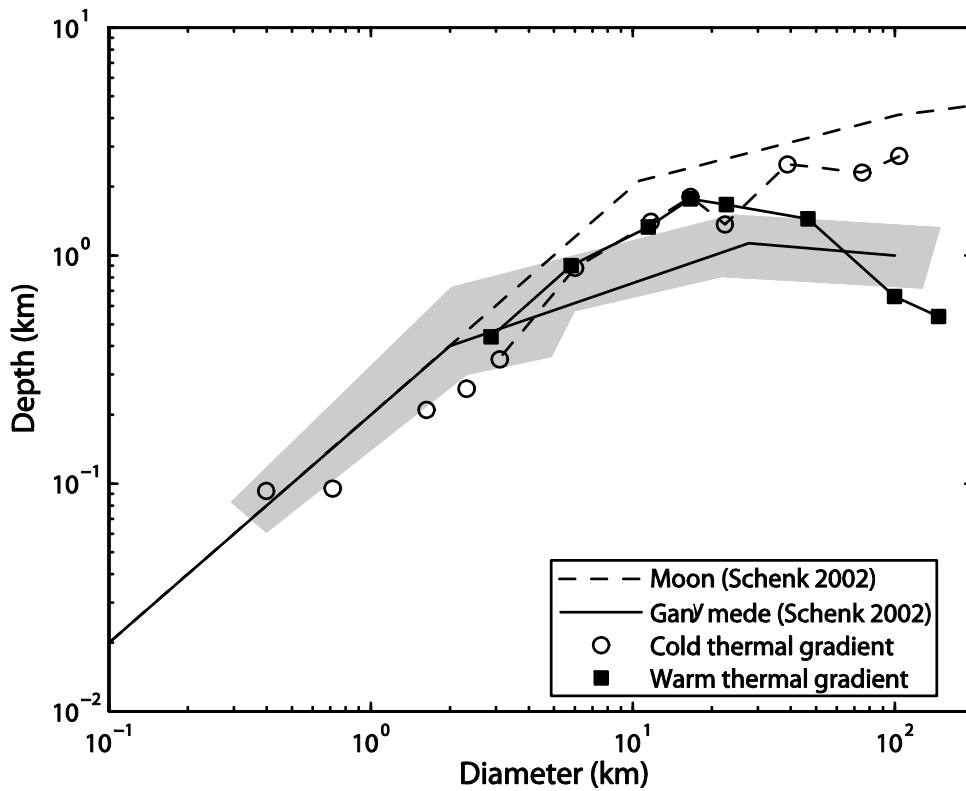


Figure 6: Depth versus diameter data for Ganymede compared with simulation results for warm and cold thermal gradients. The depth versus diameter curve for the Earth's moon is also shown for comparison (dashed line with no points). Diameters are rim-to-rim diameters and depths are rim-to-floor depths. The shaded area shows the range of measurements from Schenk (2002). Connected points are simulations that used acoustic fluidization to aid crater collapse; unconnected points utilized only the quasi-static strength model.

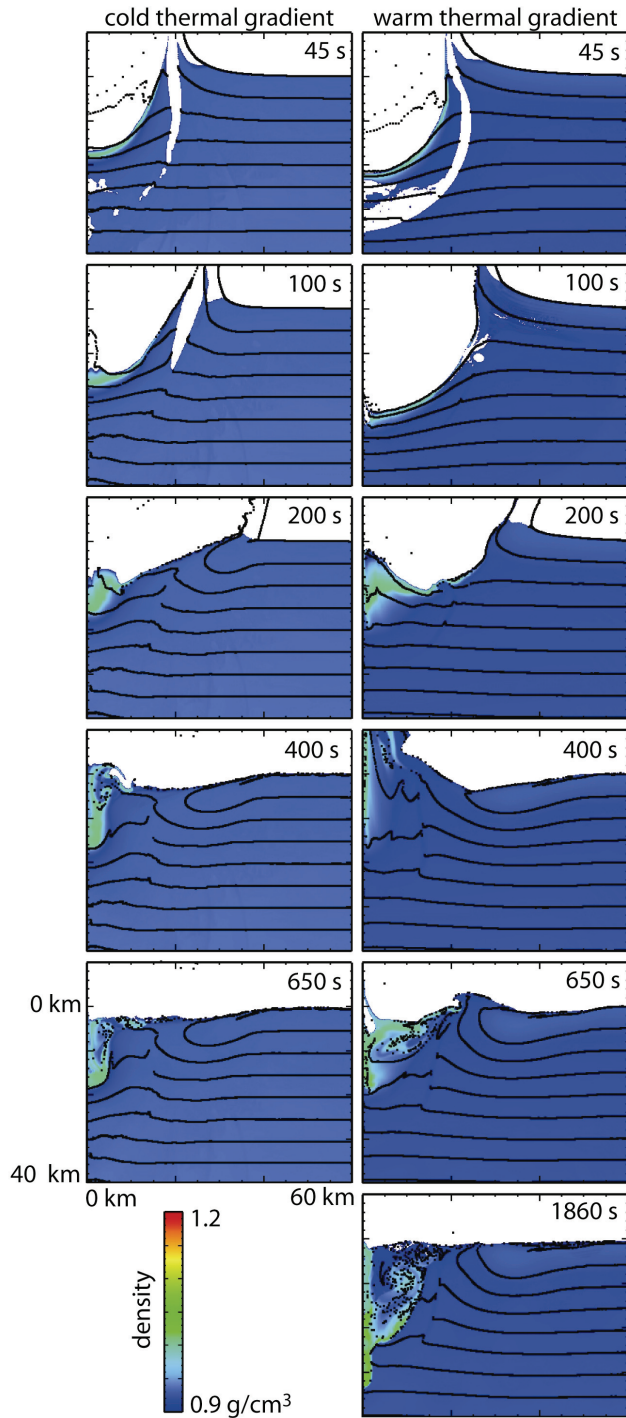


Figure 7: Time series of impacts of a 5-km diameter projectile onto Ganymede at 15 km/s with a cold (120 K isothermal) (left column) and a warm (convective) thermal gradient (right column). Stratigraphic deformation is illustrated by initially horizontal rows of Lagrangian tracer particles (black points). Colors correspond to density. The scale is the same in all panels. The final crater diameters are about 105 km (cold geotherm) and about 145 km (warm geotherm). See supplemental material for animations.

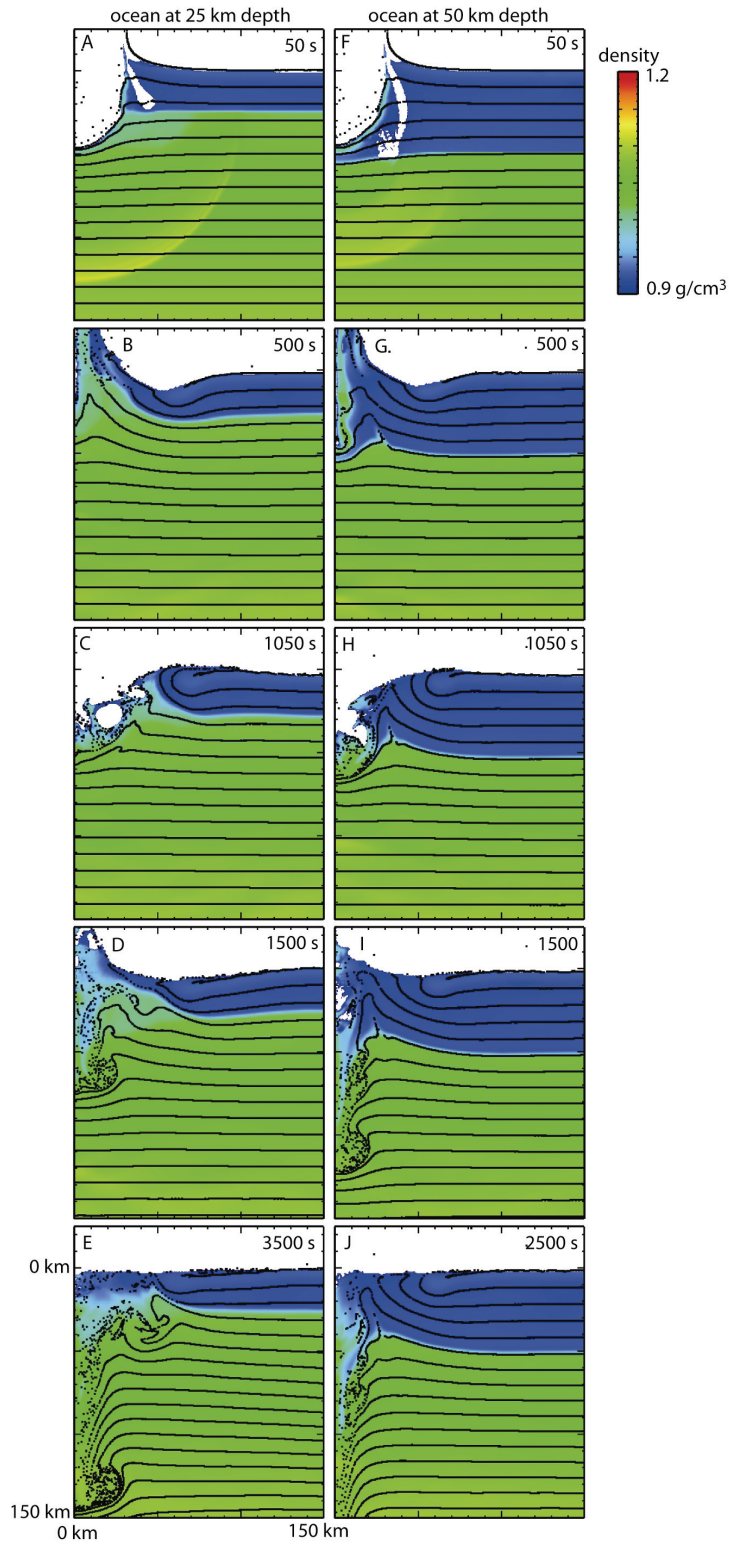


Figure 8: Time series of impacts of a 10-km diameter projectile onto Ganymede at 15 km/s with a warm thermal gradient and an ocean at 25 km (A-E) and 50 km (F-J) depth. Stratigraphic deformation is

illustrated by initially horizontal rows of Lagrangian tracer particles (black points). Colors correspond to density. The scale is the same in all panels. See supplemental material for animations.

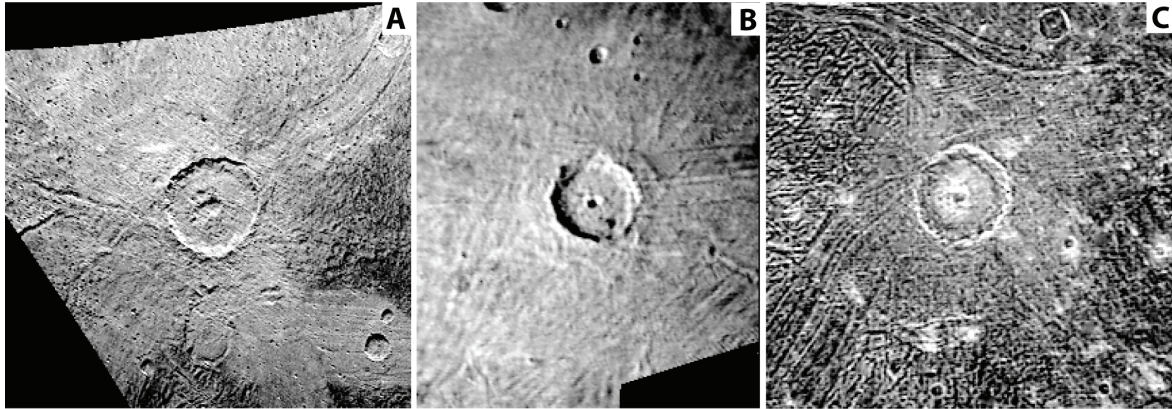


Figure 9: Examples of central pit craters on Ganymede: Isis crater, 73 km in diameter (A); Sebek crater, 64 km in diameter (B); and Bes crater, 62 km in diameter (C). (Voyager images FDS 20640.33, 16405.48, and 20637.41.)

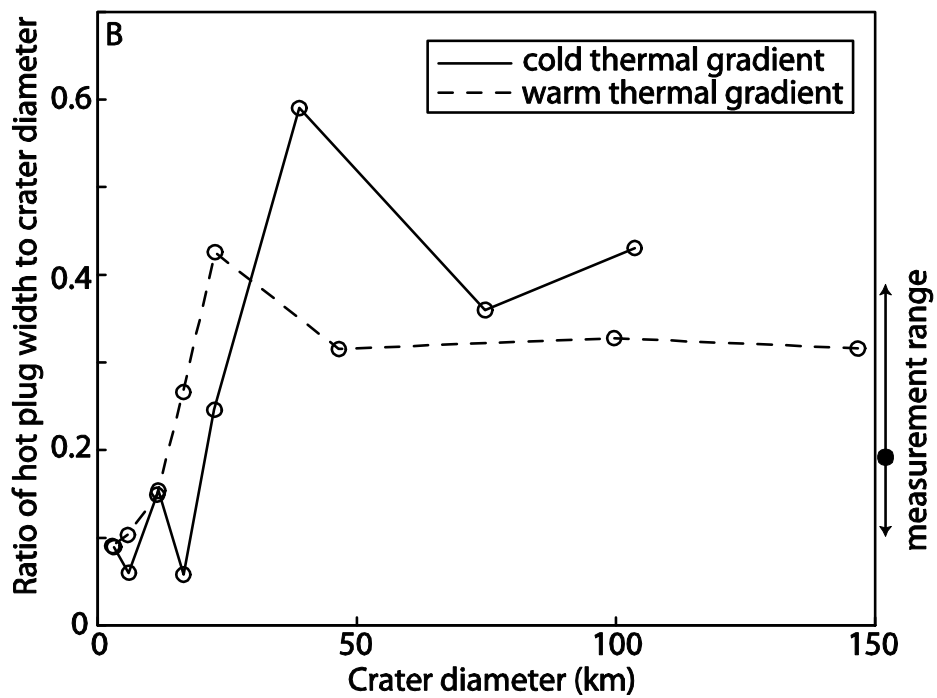
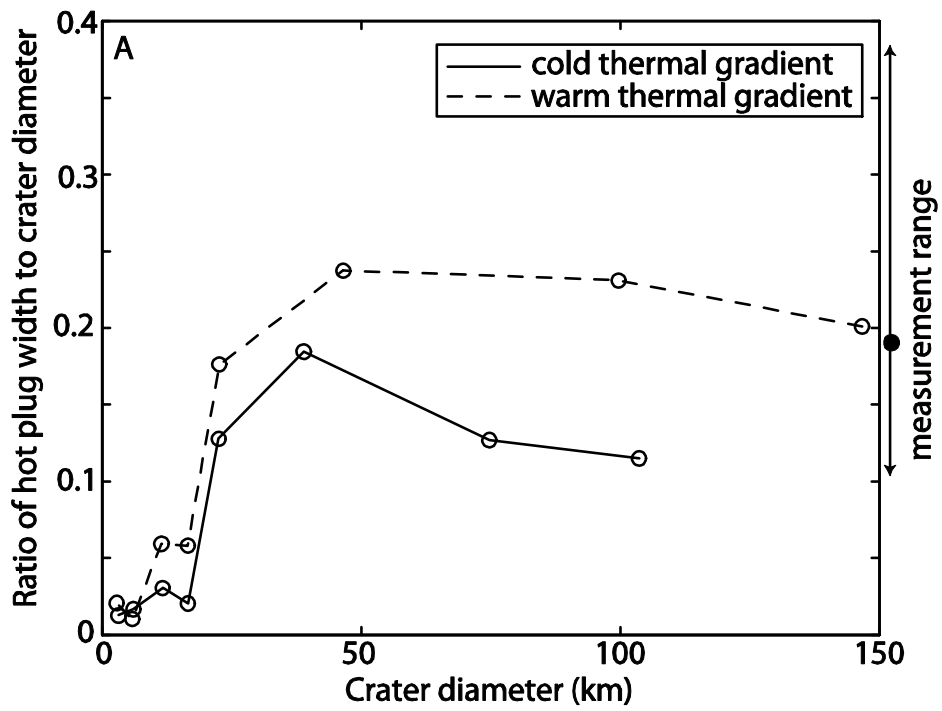


Figure 10: Ratio of hot plug width to crater diameter versus crater diameter for a cold and warm thermal gradient. In A, plug width is defined as the width of the part of the plug that extends to depth, labeled B in Figure 3C. In B, plug width is defined as the width of the plug at the surface, labeled A in Figure 3C. Arrows on the right show the range of central pit diameter to crater diameter ratios found on Ganymede (0.11-0.38), and the dot shows the mean (0.19). Ganymede data is from Alzate and Barlow (2011).

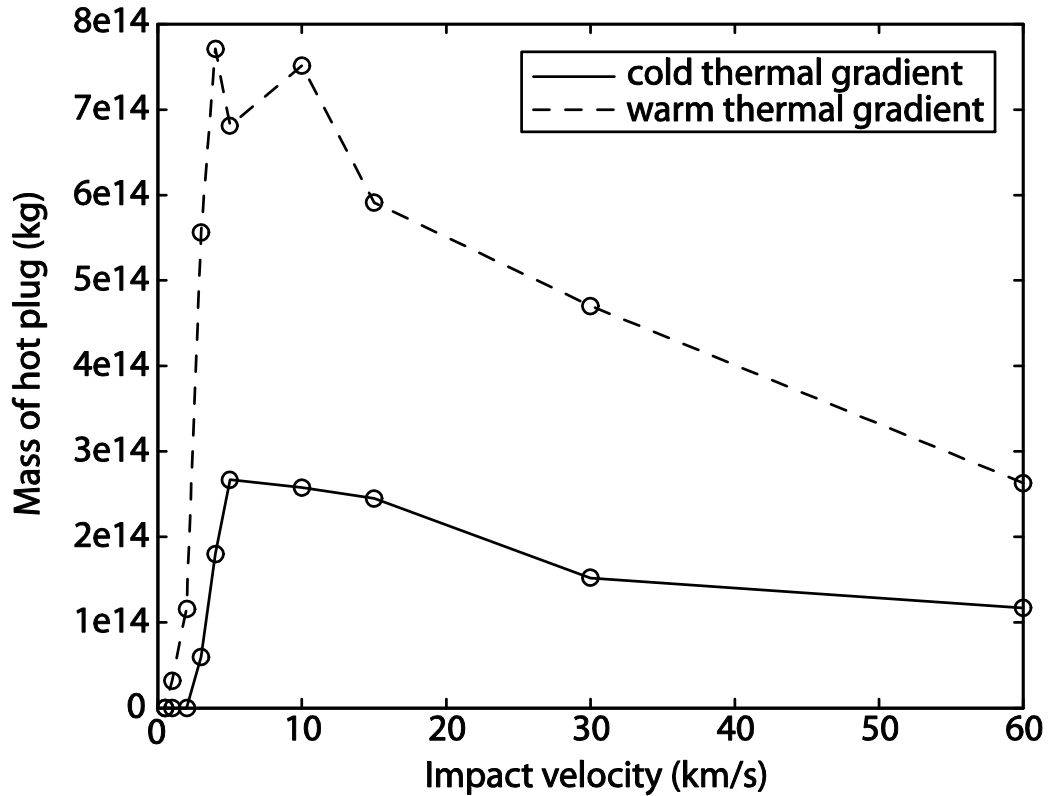


Figure 11: Mass of hot plug versus impact velocity for impacts onto a target with a warm and a cold thermal gradient. The impactor size was varied such that the amount of kinetic energy was the same. For the 15 km/s impacts, the impactor was 2 km in diameter.

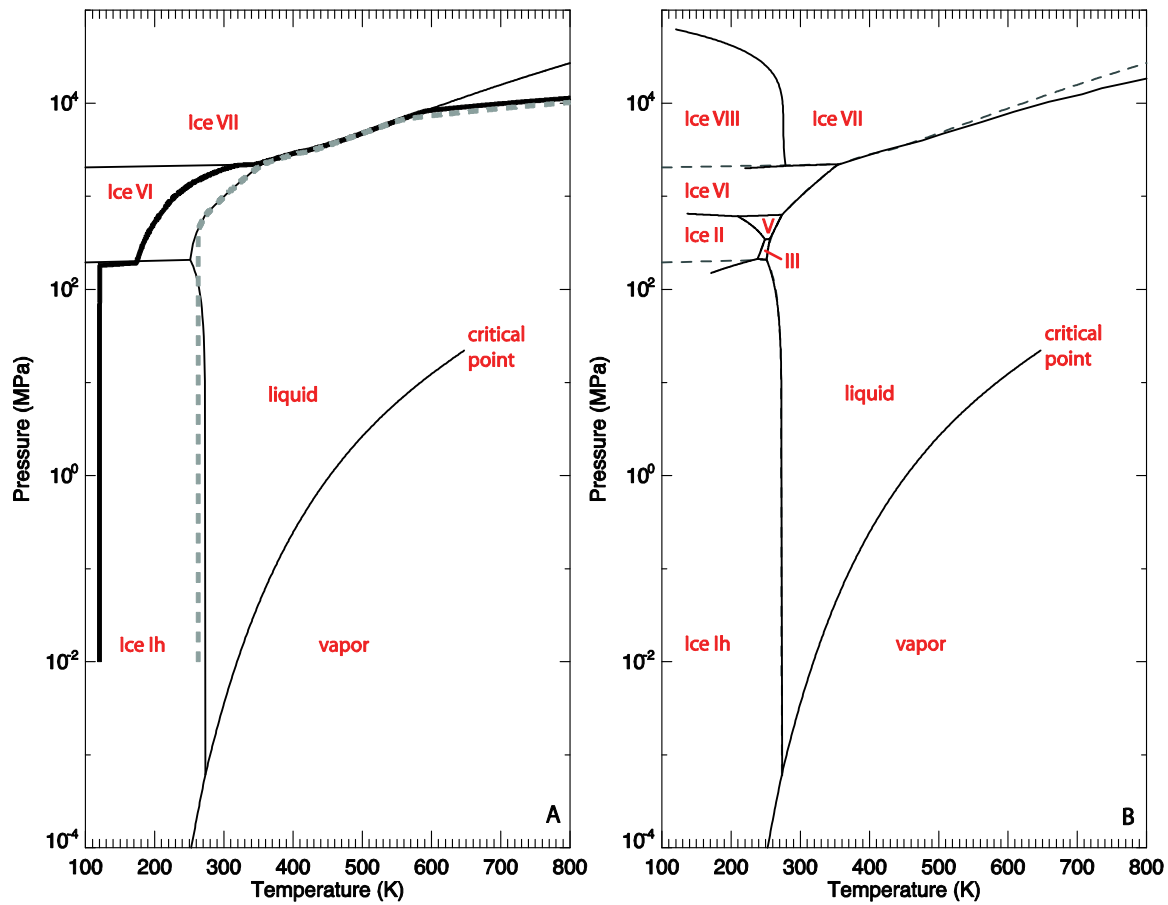


Figure A1. Comparison of 5-phase equation of state model with experimental phase boundaries of H₂O. A. Model phase boundaries with model ice Hugoniots starting at 120 K (thick black line) and 263 K (grey dashed line). B. Experimental phase boundaries as summarized in Dunaeva et al. (2010), Feistel and Wagner (2007), and Wagner and Pruss (2002). Model boundaries that deviate from experiments are shown as grey dashed lines.

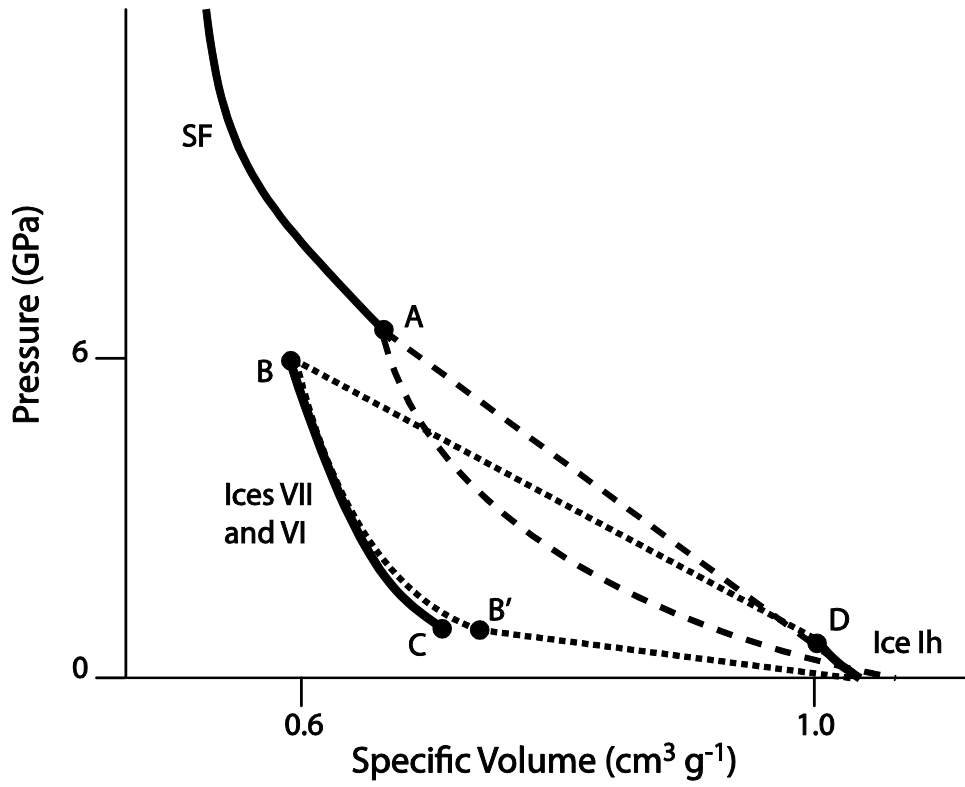


Figure A2. Schematic of the H₂O ice Hugoniot (thick line segments). Example loading and release paths are illustrated for ice shocked to the supercritical fluid (SF) phase boundary (point A, dashed lines) and ice VII (point B, dotted lines).

Variable	Description	Ice Parameters
Y_o	shear strength of intact rock at zero pressure and low temperatures	10 MPa
Y_m	limiting shear strength as pressure increases at low temperatures	115 MPa
Y_c	cohesion at zero pressure and low temperature	0 MPa
μ_i	coefficient of internal friction of intact rock	2.0
$\mu_{d,l}$	coefficient of friction of fragmented rock (low pressure)	0.55
$\mu_{d,h}$	coefficient of friction of fragmented rock (high pressure)	0.2
$P_{tr,a}$	transition pressure between $\mu_{d,l}$ and $\mu_{d,h}$	10 MPa
T_m	melting temperature	273.15 K until 623 MPa, then increases at a rate of 27.19 K/GPa
ξ	thermal softening parameter	1.84
Y_{to}	maximum tensile strength	-0.17 MPa
P_{bd}	brittle to ductile transition pressure	498 MPa
P_{bp}	brittle to plastic transition pressure	508 MPa
K_o	bulk modulus at ambient pressure and temperature	8.9 GPa
G	shear modulus at ambient pressure and temperature	3.52 GPa
D_{so}	initial shear damage	0.0
D_{to}	initial tensile damage	0.0
η	acoustic fluidization viscosity	$0.1 * C_s * r_p * \rho$
τ	acoustic fluidization decay constant	$150 * \left(\frac{r_p}{C_s}\right)$
C_{vib}	maximum vibration particle velocity (fraction of the maximum velocity)	0.25

Table 1: Quasi-static strength and acoustic fluidization parameters used to model H₂O ice. r_p is the radius of the projectile, C_s is the sound speed in ice (2.3 km/s), and ρ is the density of ice (0.932 g/cm³). For a complete description of the strength model, refer to Senft and Stewart [2007].